Journal of Environmental Chemical Engineering 11 (2023) 109311

Contents lists available at ScienceDirect

Journal of Environmental Chemical Engineering

journal homepage: www.elsevier.com/locate/jece

Hydrogen and valuable liquid fuel production from the in-situ pyrolysis-catalytic steam reforming reactions of cellulose bio-polymer wastes dissolved in phenol over trimetallic Ni-La-Pd/TiCa nanocatalysts

Walid Nabgan [a,*], T.A. Tuan Abdullah [b,*], M. Ikram [c,*], A.H.K. Owgi [b], A.H. Hatta [b], M. Alhassan [b], F.F.A. Aziz [b], A.A. Jalil [b], Thuan Van Tran [b,d], Ridha Djellabi [a]

[a] Departament d'Enginyeria Química, Universitat Rovira i Virgili, Av Països Catalans 26, 43007 Tarragona, Spain
[b] Faculty of Chemical and Energy Engineering, Universiti Teknologi Malaysia, 81310 Skudai, Johor, Malaysia
[c] Solar Cell Applications Research Lab, Department of Physics, Government College University Lahore, 54000 Punjab, Pakistan
[d] Institute of Applied Technology and Sustainable Development, Nguyen Tat Thanh University, 300 A Nguyen Tat Thanh, District 4, Ho Chi Minh City 755414, Viet Nam

ARTICLE INFO

Editor: P. Fernández–Ibáñez

Keywords:
Cellulose
Bio-polymer
Trimetallic
Ni-La-Pd
Hydrogen

ABSTRACT

Hydrogen and liquid fuel production from biopolymer waste, such as cellulose dissolved in phenol, was investigated using in-situ pyrolysis-catalytic steam reforming conditions. Developing a sustainable method for the thermal cracking of such biopolymers still faces difficulties due to the catalyst stability primarily impacted by coke deposition. The key to the proposed method is improving a highly active and stable catalytic reforming process in which trimetallic Ni-La-Pd supported on TiCa acts as a primary reforming catalyst. Catalysts were prepared by hydrothermal, and impregnation techniques, and the physicochemical characteristics of the fresh and spent materials were examined. The results showed that the NLP/TiCa catalysts performed effectively due to their comparatively high surface area, strong basicity, evenly distributed Pd particles, and appropriate redox and desorption characteristics. The addition of Pd retards the reducibility of the NL/TiCa; therefore, a Pd*La, La*Ni, La*Ti, and Ca*Ti interaction exist. Almost complete conversion of phenol (98.7%) and maximum H_2 yield (99.6%) were achieved at 800 °C for the NLP/TiCa. These findings give an insight into industrial-scale development. They have significant potential for enhancing the generation of hydrogen and liquid products from phenol and cellulose waste, such as propanol, ethanol, toluene, etc.

1. Introduction

Biopolymers are gaining traction in plastics because of their inherent biodegradability and unique characteristics for particular applications. Biopolymers may be taken from nature, biosynthesized by live organisms, or chemically synthesized from biological components. Biopolymer waste disposal is now one of the most significant worldwide issues confronting humankind and ecological balance. As the world's population continues to rise, so does the need for the polymer to meet the rising consumption levels, resulting in a severe environmental problem caused by the buildup of biopolymer waste. Biopolymer pyrolysis, a well-known technique for producing usable liquid fuels from low-value polymeric wastes, has fewer greenhouse gas emissions than other technologies, such as incineration and gasification. Bio-based polymers may be made from a variety of renewable sources. Plant-based precursors have made bio-based polymers, including lignocellulose fibers, cellulose esters, polylactic acid, and polyhydroxyalkanoates [1]. One of the abundant biopolymers is cellulose, produced from many living organisms, including plants, animals, bacteria, and certain amoebas. Organic materials/precursors with high amounts of cellulose and other fibers are chosen because they improve their mechanical intensity [2]. Food and agriculture waste are an appealing source of cellulose for industrial applications since it does not endanger the food supply and boosts the local economy [3,4].

An interesting alternative to the direct treatment of cellulose is the cracking of solutions where the cellulose is dissolved in a solvent. The influence of the solvent during the thermal degradation of polymers is significant. A proper solvent medium must be used to break the plastic waste into low molecular-weight products. Solvents that may donate hydrogen, in particular, participate in the thermal breakdown of

* Corresponding authors.
E-mail addresses: walid.nabgan@urv.cat (W. Nabgan), tuanamran@utm.my (T.A. Tuan Abdullah), dr.muhammadikram@gcu.edu.pk (M. Ikram).

https://doi.org/10.1016/j.jece.2023.109311
Received 27 October 2022; Received in revised form 21 December 2022; Accepted 11 January 2023
Available online 13 January 2023

polymers, which impacts the generation and dispersion of hydrocarbons [5]. One of The polar functional groups allows plastics to be solvated by polar solvents like carbolic acid (phenol). The phenol molecule comprises two hydroxyl (−OH) groups attached to a phenyl group ($-C_6H_5$), making it an aromatic organic chemical that is volatile. Although most microorganisms are poisonous to phenol, it is often found in many industrial effluents and is frequently utilized as broad-spectrum disinfection [6,7]. Therefore, the presence of phenolic compounds in aquatic environments is unpleasant and unwanted and dangerous to animal and human health [8]. Phenolic constituents often result from the production of petrochemical by-products [9] and makeup around 38% of the unwanted pyrolysis oil ingredient [10]. Phenolic compounds can be extracted from bio-oil by a method such as the liquid-liquid extraction technique because its presence reduces the bio-oil quality and causes high viscosity, high acidity, corrosiveness, low heating value, and faulty product that harms machinery [11]. Thus, it is environmentally favorable to utilize the phenolic compounds as a cellulose solvent using an appropriate method not only for liquid fuel generation but also for carbon-free gas fuel (hydrogen) production due to hydrogen bonds.

Polymer pyrolysis is a well-known process for producing valuable liquid fuels and has fewer greenhouse gas net emissions than other contemporary technologies like incineration and gasification and is a valuable method for chemical recycling, which lowers the carbon footprint of polymers. It can mitigate the adverse environmental effects of current management practices via landfilling and incineration and partially reduce carbon emissions while manufacturing virgin polymers. As we used a hydrocarbon solvent with six hydrogen atoms, hydrogen can also be produced, which significantly enhances the yield of generated H_2 gas during the reaction. A few technologies have also been employed for H_2 generation from bio-oil derivatives, such as dry reformation, partial oxidation, and auto-thermal reformation. Steam reforming is the most efficient and practical technique for producing hydrogen from hydrocarbons [12,13]. Compared to traditional reforming processes, the steam reforming reaction might well be conducted at significantly lower reaction temperatures, lowering the risk of catalyst carbonization and sintering and capital and operating costs. Additionally, most of the heat needed for the endothermic reforming processes is provided by the heat emitted by the exothermic carbonation reaction. Therefore, we conducted the in-situ catalytic steam reforming of phenol coupled with cellulose thermal cracking (or pyrolysis). Phenol has been used in many of previous research as a source for hydrogen production [9,14,15]. However, a significant obstacle to phenol steam reforming is the endothermic nature of the process, which has a complex of numerous side reactions, including phenol breakdown, which produces carbon dioxide, carbon monoxide, and most significantly and negatively, coke [16]. This issue can be solved by developing suitable, active, and stable nano-sized catalytic materials for the pyrolysis-catalytic steam reforming reaction.

A catalyst is any chemical compound that reduces the activation energy to speed up chemical reactions like steam reforming and thermal cracking without being wasted during the reaction. Various transition metals such as nickel [17], cobalt [18], lanthanum [19], molybdenum [20] and tungsten [21] and noble metals like rhodium [22], platinum [23], ruthenium [24], palladium [25] and supports such as alumina [26], titanium [27], calcium [28] and etc have been studied to produce hydrogen from reforming reaction of various feedstock. The availability, affordability, chemical safety, and stability of a reducible metal oxide like titanium dioxide (TiO_2) make it exceptional support [29,30]. However, it experiences coke formation, which has a negative impact on its long-term H_2 generation sustainability [14]. The CaO may be put on the appropriate support to get around this restriction and improve stability [31]. Additionally, the CaO alone suffers from cyclic instability and severe attrition loss in the reaction due to its weak mechanical strength. The mechanical strength and cyclic stability of CaO materials can also be improved by introducing TiO_2 to ensure the sustainability of H_2 production. Due to their superior physicochemical characteristics, we discovered in our earlier study [31] that equal ratios of Ti and Ca showed bifunctional capabilities, had both basic and acid phases, and had a variety of impacts on the catalyst activity in the transesterification process. The carrying capabilities of both heterogeneous and homogeneous catalysts allow transition metal catalysts to be employed as hybrid catalysts [32]. Because of their low price especially in comparison to catalysts like Rh, Ru, or Pt, as well as their effectiveness for C–O, C–H, and C–C bond breakage and water gas shift reaction, which was caused by the high Lewis acidity intensity of nickel metal, nickel-based catalysts have been explored more in-depth for the removal of tar [33,34]. However, the supported mono-metallic nickel (Ni) catalyst often experiences quick deactivations brought on by the sintering of Ni nanoparticles (NPs) and the accumulation of coke [35]. Adding a second active metal to a bimetallic catalyst uses the synergy between the active metals, often transition metals, to increase coke resistance and active phase dispersion. We have illustrated that this issue of nickel can be solved by introducing another transition metal in the catalyst with great resistance to carbon [16,36]. The enhanced coking resistance of the bimetallic and trimetallic catalysts may be attributed to changing the electronic structure of the catalyst. The advantages of lanthanum (La_2O_3) as promoters were determined by steam reforming of the bio-aqueous oil's component [18]. La_2O_3 is intended to increase the distribution of active metal particles on the support and decrease the agglomeration of such materials throughout reforming. Additionally, because of the increased mobility of lattice oxygen anions, it may reduce the formation of coke [19]. La_2O_3 enhances the catalyst's thermal stability and modifies the acidic and basic characteristics of compounds [37]. Ni and La are examples of transition bimetallic NPs with large surface area and energy, making them effective catalysts. In a bimetallic Ni-La catalyst, the strong oxygen affinity of La promotes carbon oxidation and minimizes coking, while hydrogen overflow from Ni to La limits its oxidation. Despite the encouraging results for bimetallic catalysts [10,25,27,35], the catalyst's stability for extended periods of time in the stream during cellulose cracking at high temperatures has to be clarified. Additionally, the overall surface area and activity of these catalysts are significantly impacted by the coking and sintering of relatively large metal particles [38], particularly when it comes to the heat breaking of polymer bonds. Therefore, it is thought to be desirable to promote the bimetallic active transition metals by a little quantity of noble metal in order to profit from their higher coking resistance and stability while reducing the problem of their high cost and scarcity [39]. The hydrogen spillover mechanism, which accounts for the lowering of the reduction temperature by noble metal promotion, states that as hydrogen adsorbs and dissociates on noble metals, the adsorbed hydrogen atoms disperse on the support surface to reach non-noble metal species, boosting their reduction. Additionally, morphology and composition of the noble metals catalysts are crucial factors that affect their catalytic activity and stability. Since they have the capacity to dramatically alter the catalytical structure and effect performance, their partial application is economically feasible even at low concentrations (~1 wt%) [40]. When Pd NPs had rough surfaces, dendritic topologies, or porous architectures, for instance, they outperformed their compact counterparts in terms of catalytic efficacy [41]. To improve the catalytic performance, the porous structure may provide a significant specific area, many exposed active sites, and an effective diffusion channel for molecules and electrons. As Pd promoters have attracted great interest, we also targeted the in situ hydrogen production reaction by employing a small amount of Pd in our previous work with remarkable increase in the catalytic activity [25,42]. Pd promoters are good substrate components for customized multimetallic catalysts for hydrogen generation provided the control mechanisms learned, and their increased thermal stability is boosted by a strong metal-support interactions.

Despite the evidence disclosed in previous research regarding trimetallic catalysts, there is still a lack of investigations on developing trimetallic nanosized catalysts to crack and reform the cellulose bonds and phenol compound to liquid fuels and hydrogen gas in the scientific

literature. To increase the feasibility of this study and increase the ratio of the cellulose to solvent to 2:8, which is much higher compared to our previous works [43–45], we modified the experimental setup and connected a Parr Benchtop Reactor (PBR) (see Fig. 1). This modification allows the easily liquefying and increasing of the amount of polymer and plastic waste in the reaction without causing line blockage. The novelty of the work also lies in developing an understanding of the role of the trimetallic Ni-La-Pd catalyst supported on TiCa for hydrogen production and liquid fuel generation from cellulose dissolved in phenol in the unique process conditions of the in-situ pyrolysis-catalytic steam reforming. Four catalysts were synthesized by hydrothermal treatment methods followed by conventional impregnations method and named as TiCa (ratio 1:1), N/TiCa (Ni to TiCa ratio is 1:9), NL/TiCa (Ni:0.7, La:0.3, TiCa:9), and NLP/TiCa (Ni:0.6, La:0.25, Pd:0.15, TiCa:9) nanocatalysts. The physicochemical characteristics of the fresh catalyst were examined XRD, BET, N_2 adsorption-desorption isotherm, NH_3-TPD, IR-Pyridine, IR-Pyrrole, H_2-TPR, CO_2-TPD, FTIR-KBr, TEM, EDX, HRTEM, SAED, Elemental mapping analysis, and ICP test. Catalysts were screened at 600 °C, the optimum catalyst was tested at 500–800 °C, and stability was studied for 72 h on stream. GC-TCD characterized gaseous products, and liquid fuels were also examined by GC/MS, GC-FID, and FTIR. The catalysts were analyzed by TGA-DTG, BET, N_2 adsorption-desorption isotherm, TEM, FTIR-KBr, and CHNS.

2. Materials and methods

2.1. Preparation of NiLaPd/Ti-Ca nano-catalysts

The nanosized TiCa support hydrothermal followed by impregnation route and followed our published works [31,44]. A particular amount of CaO and TiO_2 were combined with 100 mL of deionized water for dilution purposes and with the 1:10 mass ratio and agitated for a couple of hours, separately in two separate beakers, after 5 M of sodium hydroxide (NaOH) had been dissolved and mixed for an hour. The NaOH was employed to improve the nucleation and growth rates of the NPs [46]. A 100 mL Teflon container was used to contain the fluid. Then, an autoclave made of stainless steel was firmly sealed and housed two Teflon bottles filled with these solutions. The autoclave was put into a temperature-controlled electric oven and hydrothermally treated for 48 h at 160 °C. The treated sample was filtered and washed with distilled water several times and dried at 110 °C overnight. The prepared TiCa sample was calcined in an oven (Model Ney Vulcan D-130) at 800 °C for 3 h. The synthesis steps for each catalyst are depicted in Fig. S1.

The monometallic N/TiCa nanocatalyst was prepared in the same steps as the TiCa nanocatalyst. Firstly, a specific amount of nickel nitrate hexahydrate and then 5 M NaOH were dissolved in 100 mL deionized water at room temperature for an hour until a homogenous and clear solution appeared. Subsequently, the solution was transferred into an autoclave reactor equipped with a 100-mL Teflon cylinder and kept in the oven for 48 h at 160 °C. The powder containing Ni NPs was then washed via filter paper on a Buchner funnel that was sealed with a rubber bung on the top of a side arm conical flask. The side arm of the flask was connected with a vacuum pump to speed the filtration and washing process of the samples, followed by drying at 110 °C overnight and then calcination for three hours at 800 °C. The Ni NPs supported on TiCa nanosized support with a volume ratio of 1–9 were prepared via impregnation. Briefly, after gently adding the prepared TiCa material into 150 mL of a beaker filled with deionized water, the Ni powder was introduced to the solution and kept stirring on a hot plate stirrer at 90 °C until water vaporized. The slurry was dried at 110 °C overnight and then calcination for three hours at 800 °C. The same procedure was employed for synthesizing La NPs by hydrothermal treatment method and then impregnating La into N/TiCa to produce a bimetallic NL/TiCa nano catalyst. Trimetallic NLP/TiCa nanocatalyst (Ni:La:Pd:TiCa ratio is 0.6:0.25:0.15:9) was prepared in the same way as the monometallic and bimetallic ones, replacing the TiCa support by a bimetallic NL/TiCa nanocatalyst.

2.2. Characterization of the nanocatalysts

The crystalline structure of the catalysts was characterized by X-ray diffraction (XRD) conducted on a D8 ADVANCE Bruker diffractometer equipped with Cu Kα radiation (λ = 0.154 nm, Philip), 40 kV and 30 mA. The Fourier-transform infrared (FTIR) spectra (from 4000 to 400 cm^{-1}) were collected on a Shimadzu IR-Prestige-21 spectrometer to examine functional groups in the synthesized and used catalysts. Before measurement, the samples were diluted with potassium bromide (KBr)

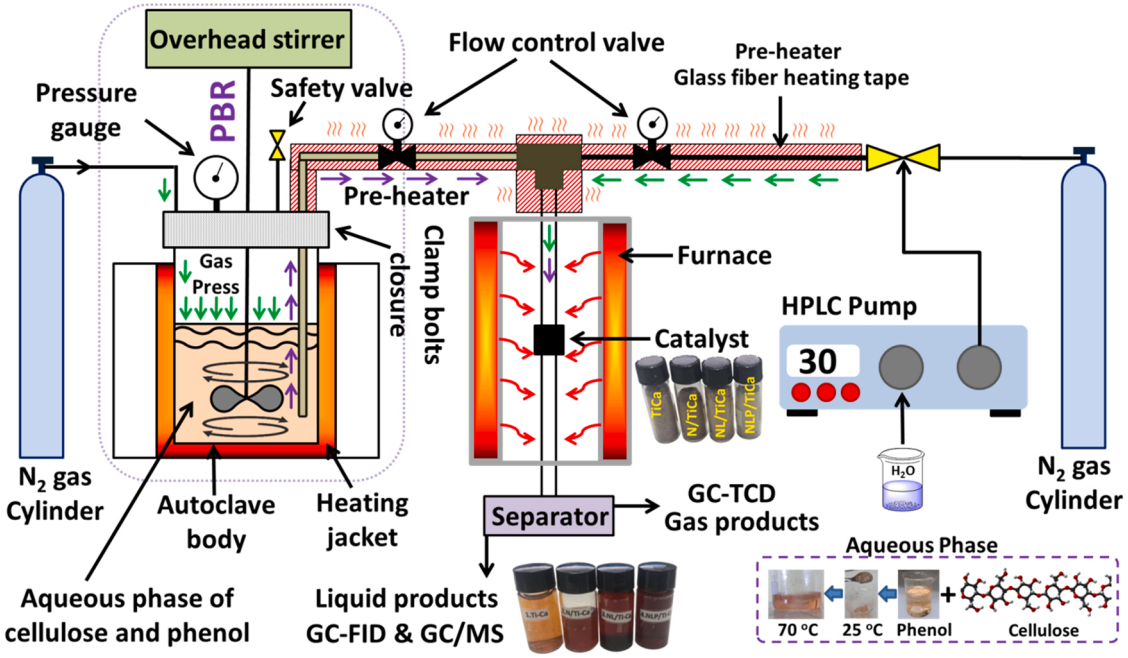

Fig. 1. A schematic flowcharts for the steam reforming and catalytic cellulose-phenol cracking reactor.

and pressed into pellets. The KBr pellet was prepared by mixing KBr and catalyst (1 (mg):100 (mg)), and the excellently designed combination was pressed to procedure a 13 mm diameter pellet. N_2 adsorption-desorption isotherms of the fresh and used samples were obtained at − 196.1 ºC over the whole range of relative pressures using a Beckman Coulter SA3100™ instrument. Before N_2 adsorption-desorption measurements, samples were degassed at 180 °C in a vacuum for 12 h. Specific surface areas (S_{BET}) of the fresh and used samples were calculated by the Brunauer-Emmet-Teller (BET) equation, considering the range of relative pressures $0.1 < P/P_o < 0.3$. Barrett-Jouner-Halenda (BJH) technique was used to compute pore size and volume from the desorption branch of the isotherm, and the BET method was used to estimate surface area. The elemental composition of the catalysts was detected using inductively coupled plasma (ICP-test) on the Agilent ICPOES720. A JEOL JEM-ARM200F apparatus operating at 200 kV was used to capture the samples' transmission electron microscope (TEM) and high-resolution transmission electron microscopy (HRTEM) micrographs. The same instrument was employed for the Energy Dispersive X-Ray (EDX) elemental analysis and crystallographic experimental analysis by the selected area diffraction (SEAD) technique. Temperature-programmed reduction (TPR) scans were performed to study the catalyst's reducibility in a Micromeritics Chemisorb 2720 apparatus. Approximately 100 mg of the precursor material and a flow of 20 mL/min of pure hydrogen, with a 20 °C/min heating rate, were used for the tests. Using the Micromeritics Chemisorb 2720 apparatus, temperature-programmed desorption of ammonia (NH_3-TPD) was carried out to investigate acidity. The material was pre-treated in He flow at 200 °C for 30 min before being admitted with ammonia. Following cooling to room temperature, the sample was exposed to a stream of pure NH_3 (20 mL/min) for 30 min. The sample was purged in flowing He (20 mL/min), and the temperature of the catalytic sample was then raised to 900 °C (T = 20 °C/min), removing the physically adsorbed ammonia. The surface acidity and the evaluation of the catalysts' protonic and Lewis acid sites and the supports were also investigated by means of an FTIR spectroscopic study of adsorbed pyridine as a probe molecule. Pyridine (2 Torr) was first adsorbed for 30 min at 423 K, then released for the same amount of time at 500 °C. The analysis was done using a Cary 640 FTIR spectrometer (Agilent, Selangor, Malaysia) with CaF_2 windows and a stainless steel cell that can withstand heat. The pelletized material was activated for one hour at 400 °C before pyridine adsorption. After that, the sample was heated to 150 °C while being exposed to pyridine (4 Torr), and the spectra were then gathered at room temperature. To investigate catalysts' basicity, temperature-programmed desorption of carbon monoxide (CO_2-TPD) experiments were conducted using the same apparatus and procedures of NH_3-TPD analysis except with the replacement of NH_3 by CO_2 flow. The fundamental characteristics of the catalyst were further characterized using pyrrole-probed IR spectroscopy. On an Agilent Cary 640 FTIR spectrometer with a high-temperature stainless steel cell and CaF_2 windows, in situ FTIR was used to accomplish the experiments. All samples underwent a 1-hour activation period at 500 °C before the measurements. The activated catalyst was then outgassed at room temperature for 15 min after being exposed to 4 Torr of pyrrole for 15 min. Three scans were used to capture each spectrum at ambient temperature with an aspect ratio of 8 cm^{-1}.

The amount and type of coke formation on the catalysts after being used in the in-situ pyrolysis-catalytic steam reforming conditions were determined by thermogravimetric analysis (TGA) and derivative thermogravimetry (DTG), TEM, and CHNS (carbon, hydrogen, nitrogen, and sulfur) elemental analyzer. The TEM images of the used catalyst were conducted with a JEOL JEM-1011 microscope that functioned at 80 kV. TEM specimens were equipped by dispersing the catalyst powder in acetone with sonication and dropping it onto an ultrathin carbon-coated copper grid. The TGA analysis was performed using the Shimadzu TG-50 instrument in a nitrogen flow at a heating rate of 20 °C/min.

2.3. Catalyst screening

The experimental setup for the in-situ pyrolysis-catalytic steam reforming reactions is mainly comprised of two reactors, and the setup is shown schematically in Fig. 1. The first is a Parr Benchtop Reactor (PBR) equipped with a stir-shaft, a pressure gauge, an autoclave body, a sampling tube, a safety valve, a heating jacket, and a thermocouple thermometer. The PBR is installed to homogenize the liquid phase of the high volume of cellulose in the phenol (2:8) at 70 °C and pressurize the solution with the N_2 gas into the fixed bed reactor. The exit line of the PBR is swathed with glass fiber heating tape to vaporize the liquid before entering into the second reactor that is responsible for catalytic testing. The water line before the reactor was also preheated to 200 °C so that the water could first vaporize before being mixed with the gas phase of the cellulose and phenol. A vertical tube reactor with an inner diameter of 8 mm and a length of 300 mm was used for the catalytic testing, and it was situated within a furnace with a heating zone. Before the reaction, 0.2 g of catalyst powder was in-situ reduced at 600 °C for 1 h in pure hydrogen 30 mL/min flow after being fixed in the reactor's center using layers of quartz cotton at atmospheric pressure. After reduction, the reactor was purge-gassed with pure nitrogen for a time to clear out any excess reducing gas. A mass-flow controller system was used in each test to regulate the feeding stream. The thermocouples were positioned in the middle of the inflow area of the fixed bed reactor and were used to monitor the pressure, flow rates, and temperature continually. After the reaction, condensable molecules were liquefied by a glass coil heat exchanger equipped with a chiller at 10 °C. The gas reactor effluent was analyzed online employing a GC-TCD (Agilent 6890 N), and the liquid product was analyzed using a GC-FID (HP 5890 Series II) equipped with a 0.53 mm x 30 m CP-Wax capillary column and GC/MS (Agilent 7890B). Each run was repeated at least six times to ensure accuracy and reproducibility. The result analyses, such as phenol conversion (based on a calibration curve from GC-FID results), and produced gas composition in yield, were calculated following our previous research [25] and as shown in Eqs. (1), (2), (3), and (4).

$$Phenolconversion(\%) = \frac{[Phenol]_{in} - [Phenol]_{out}}{[Phenol]_{in}} \times 100 \quad (1)$$

$$H_2yield(\%) = \frac{molesofH_2obtained}{molesofH_2stoichiometric} \times 100 \quad (2)$$

$$COyield(\%) = \frac{molesofCOobtained}{molesofCOstoichiometric} \times 100 \quad (3)$$

$$CO_2yield(\%) = \frac{molesofCO_2obtained}{molesofCO_2stoichiometric} \times 100 \quad (4)$$

The quantity of each chemical that must react for the reaction to be fully catalyzed is known as the stoichiometric moles. So, for example, we have Eq. 5's representation of the balancing steam reforming equation.

$$C_6H_5OH + 11H_2O \leftrightarrow 6CO_2 + 14H_2 \Delta H^o = 463.65kJ/mol \quad (5)$$

$$C_6H_5OH + 5H_2O \longrightarrow 6CO + 8H_2 \Delta H^o = 710.91kJ/mol \quad (6)$$

$$CO + H_2O \leftrightarrow CO_2 + H_2 \Delta H^o = -41.15kJ/mol \quad (7)$$

3. Results

3.1. Catalyst characterization

The structural properties of calcined catalysts determined from nitrogen adsorption isotherms at − 196.1 ºC are shown in Table 1, while the adsorption-desorption isotherms curves of nitrogen at − 196.1 ºC and pore size distribution profiles of the fresh samples are presented in Fig. 2. Table 1 shows the textural properties of fresh catalysts, which were specific surface area, total pore volume, and average pore

Table 1
Metal contents (ICP test), crystal size, BET surface area, pore volume, average pore diameter, basicity, reducibility, acidity, and data of the fresh nano-catalysts.

Catalysts	Ni (wt %)[a]	La (wt %)[a]	Pd (wt %)[a]	Crystal size (nm)	S_{BET} (m^2/g)[b]	V_p (cm^3/g)[c]	D_p (nm)[d]	H_2-Consumption (mmol/g)	CO_2 uptake (μmol/g)	NH_3 uptake (μmol/g)
TiCa	0.0	0.0	0.0	120.1	6.26	0.0374	23.89	12.09	3.57	8.51
N/TiCa	9.7	0.0	0.0	91.5	11.89	0.0803	27.02	9.53	5.64	6.75
NL/TiCa	6.2	2.9	0.0	70.1	18.01	0.0685	15.22	16.79	5.50	6.84
NLP/TiCa	5.8	2.4	1.3	68.1	28.17	0.0995	14.13	19.38	4.76	2.48

[a] The metal content was measured by the ICP test
[b] S_{BET}, BET surface area
[c] V_p, total pore volume
[d] D_p, average pore diameter

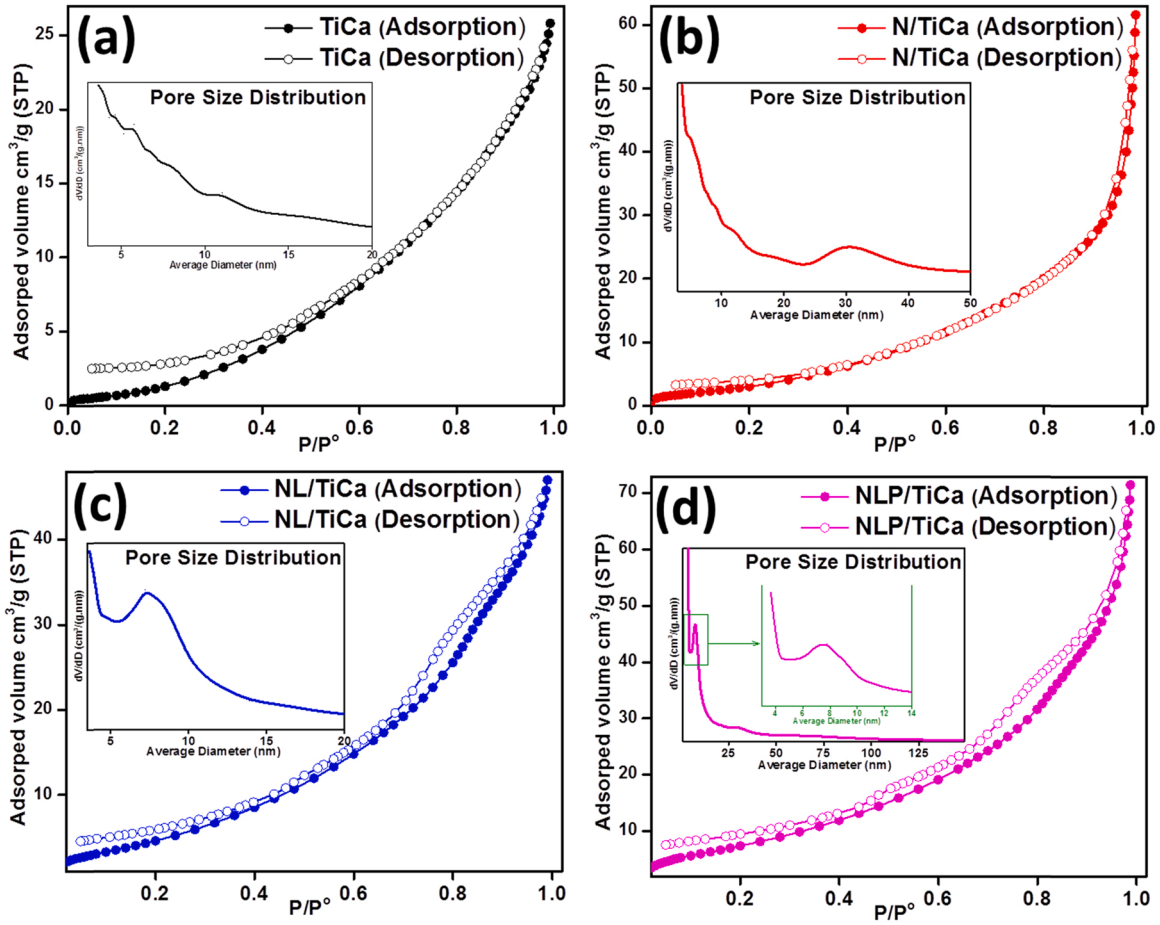

Fig. 2. Nitrogen adsorption-desorption isotherm and pore size distribution of the fresh (a) TiCa, (b) N/TiCa, (c) NL/TiCa, and (d) NLP/TiCa nano-catalysts.

diameters. The BET surface area of the TiCa catalyst is 6.26 m^2/g. After the nickel material, the surface area increased to 11.89 m^2/g, the pore volume also rose from 0.0374 to 0.0803 cm^3g^{-1}, and the average pore size reduced from 23.89 to 27.02 nm. After introducing lanthanum, the surface area increased to 18.01 m^2/g, and pore volume and average pore diameters were reduced to 0.0685 cm^3/g and 15.22 nm. The addition of transition metals significantly increased the surface areas, most probably due to the increasing metal and support interactions. When palladium was added, the surface area increased significantly (to 28.17 m^2/g), and the pore volume rose (to 0.0995 cm^3/g). It is important to note that the textural characteristics of the catalysts enhanced somewhat with the addition of the noble metals, but just a modest improvement was seen for the transition materials. The increase in the surface area and the total pore volume could also be obtained through these ways. The deposition of metal nanoparticles on the external surface leads to new adsorptive sites, which increase the adsorption of N_2 on the surface. TiCa mixed with metal nanoparticles could form a porous coordinated complex composition wherein metal NPs could be inserted between TiCa large particles (in the form of a sandwich structure). The low surface area of bare TiCa calcined at the same temperature confirmed this statement. The larger pore volume and surface area of the NLP/TiCa nanocatalyst compare to TiCa, N/TiCa, and NL/TiCa are beneficial for mass transfer, which often results in the high catalytic activity of the catalysts.

Various pore morphologies have often been linked to the geometries of hysteresis loops. As presented in Fig. 2, the N_2 adsorption-desorption isotherms of TiCa support belong to Type III (without a hysteresis loop), while the type of hysteresis loops for N/TiCa, NL/TiCa, and NLP/TiCa catalysts are Type H4 (with a significant increase in the adsorbed amount at P/P_o>0.7) according to IUPAC classification [47,48]. This

shows that it has a micro/mesoporous structure with a variety and abundance of mesopores. Adsorption was somewhat constrained at high P/P_o, which may have been brought on by the presence of non-rigid aggregates of plate-like particles or collections of slit-shaped pores [49]. According to the adsorption isotherms, monolayer adsorption forms primarily at low relative pressure, but at high relative pressure, mesopore adsorption causes the production of many layers up to capillary condensation, which results in a significant rise in adsorption volume. Finally, the isotherm reaches a plateau, and the adsorption terminates in the mesopores. Only the TiCa and N/TiCa catalysts (approximately 11 nm and 30 nm, respectively) exhibit big pores, according to Fig. 2 of the BJH pore size distribution, but the pore diameters of the NL/TiCa and NLP/TiCa catalysts are between 5 and 9 nm.

Fig. 2 shows that the bottom portion of the hysteresis loop area for this isotherm (up to 25 $cm^3.g^{-1}$ (STP)) overlaps the same region of the isotherm obtained for the TiCa nanocatalyst when the acquired isotherm is modified upward by ~2.5 $cm^3.g^{-1}$ (STP). In contrast, the top portion of the hysteresis loop area (above 60 $cm^3.g^{-1}$ (STP) for this isotherm) overlaps the same region of the isotherm for the N/TiCa catalyst when the isotherm obtained following the introduction of nickel is modified higher by 3.3 $cm^3.g^{-1}$ (STP). Also, the amount of adsorbed nitrogen at higher relative pressures (P/P_o) decreased with La doping, indicating a decrease in the mesoporous and improved in the specific surface area for the NL/TiCa nanocatalyst. This result shows that La has filled pores where capillary condensation occurs at intermediate relative pressures and that La has not interfered with the capillary condensation processes happening inside pores filling in either the higher or lower parts of the hysteresis loop. Such effects can also be attributed to the partial loading of pores and the formation of La crystallites on the external surface of N/TiCa particles. Compared to other samples, the NLP/Ti sample had the most N_2 uptake in the 0.6–0.9 (P/P_o) range, which suggests a larger mesopore volume. Increasing Pd and La modifiers loading seems to narrow the pore size distribution. The existence of Pd causes to block the pores of the catalysts, which leads to a decrease in the internal surface area. The deposition of Pd NPs on the external surface of the catalyst results in the generation of new adsorptive sites. Based on these results, we can tentatively presume that the catalyst surface area increased after loading Pd metal, which is considered beneficial for the in-situ pyrolysis-catalytic steam reforming conditions of cellulose dissolved in phenol.

Fig. 3(a) and Table 1 show the XRD pattern and quantitative data of total crystal sizes, which were obtained through the analysis of the structure of crystalline materials and the identification of the crystalline phases present in a material to reveal chemical composition information based on their diffraction pattern. Diffraction data and JCPDS (Joint Committee on Powder Diffraction Standards) were analyzed using the X′pert Highscore software. The XRD curves of all catalysts showed characteristics peaks at 2θ angles of 23.05°, 34.33°, 37.32°, 47.45°, 53.82°, 59.28°, 69.84°, and 79.45° that were signed by red hearts corresponding to 101, 210, 102, 202, 103, 042, 242, and 161 diffractions of orthorhombic phase, which are in parallel with the standard JCPDS card number 96–231–0619 for $Ca(TiO_3)$ alloy and 92.8 nm of crystal size. The XRD pattern obtained for the TiCa catalyst shows individual peak characteristics of crystallized $Ca(TiO_3)$ and equals 93.4 nm of crystal size at 2θ angles of 68.84° and corresponding to 402 crystal structure. The two diffraction peaks at 50.81° and 72.34° for the TiCa catalyst (marked with green trefoil shapes) are ascribed to 211 and 123 monoclinic structural phase of Baddeleyite (Ti_4O_8; JCPDS 96–901–5356). The intensity of the characteristic peak of the N/TiCa catalyst is weaker than TiCa; probably, it may be due to the entry of Ni into the lattice of TiCa, which could cause a formation of a new solid solution structure. The prepared samples all displayed the characteristic diffraction peaks of Ti_6O_{11} and were marked with blue diamonds (JCPDS 96–152–1096) with four prominent diffraction peaks (133.3 nm of crystal size) appeared at 30.29°, 32.17°, 64.09° and 67.34°, which could be ascribed to the 114, 206, 423, and 609 crystal planes of monoclinic Ti_6O_{11}, respectively. The diffraction peak with 2θ° values of 39.86 and marked

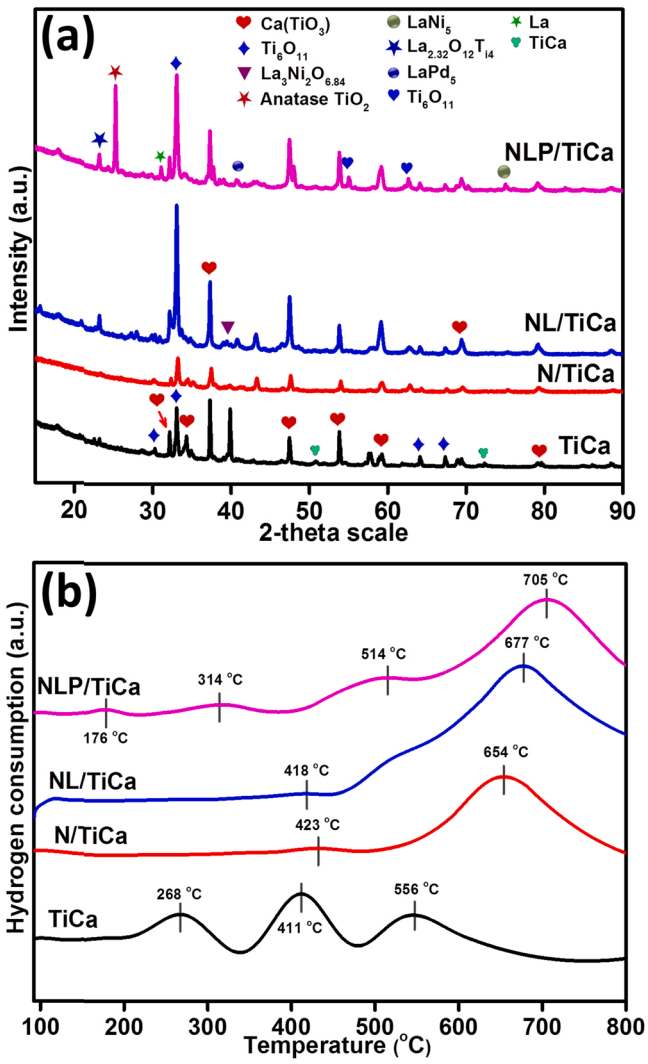

Fig. 3. (a) XRD outline for the fresh nano-catalysts, and (b) temperature programmed reduction of hydrogen (H_2-TPR) of the fresh catalysts.

with a purple triangle corresponding to $La_3Ni_2O_{6.84}$ crystal plane of 312 and 43.6 nm of crystal size, confirming $La_3Ni_2O_{6.84}$ orthorhombic structure (JCPDS 96–153–2218). After introducing La and Pd materials, multiple peaks were detected at 23.2°, 25.28°, 31.07°, 40.71°, 55.06°, and 75.04°. Clearly visible $LaPd_5$ alloy (marked by blue circles with 26.6 nm of crystal size) was confirmed by the diffraction peaks of hexagonal at 40.71°, with the corresponding 002 crystal facets (JCPDS 96–152–2598). Similar to NL/TiCa catalyst, peaks were again observed at 75.04° with green circles, which is attributed to the metallic $LaNi_5$ alloy with hexagonal phase structure of 211 and 259.6 nm of crystal structure (JCPDS 96–153–7852). The additional peak observed at 23.2° and marked with blue stars with a crystal size of 73.2 nm represents the 101 crystalline planes of $La_{2.32}O_{12}Ti_4$ orthorhombic structure (JCPDS 96–412–4542). The anatase phase structure of TiO_2 was seen at 25.258° (101) and ascribed by a red star with 89.3 nm crystal size and a JCPDS of 96–900–8215. The (102) La plane diffraction peak (with green star) observed for NLP/TiCa appeared at 31.07° with 58.9 nm (JCPDS 96–900–8526). Peaks for Ti_6O_{11} crystal (marked with blue hearts) were detected at 55.06° and 62.75°, ascribed to the 514 and 517 crystal planes of monoclinic structures (175.8 nm, JCPDS 96–152–1096), respectively. For the NLP/TiCa and NL/TiCa samples, the diffraction peak intensity of the $Ca(TiO_3)$ alloy crystal phase is enhanced. When calcination at high temperatures, the spinel NLP/TiCa and NL/TiCa might completely decompose into Ca and Ti alloy. The excellent

crystallinity and the largest surface area of NLP/TiCa nanocatalyst could be exhibited in the presents of $LaPd_5$, $LaNi_5$, $La_{2.32}O_{12}Ti_4$, and $Ca(TiO_3)$ alloys resulting from high reducibility and metal support interaction as depicted in Fig. 3(b). It is expected that the NLP/TiCa can perform an excellent catalytic activity that can be directly associated with the catalyst's physical characteristics, such as crystallinity and surface area.

The catalytic characteristics of transition and noble metal NPs deposited on TiCa may sometimes also be described in terms of the

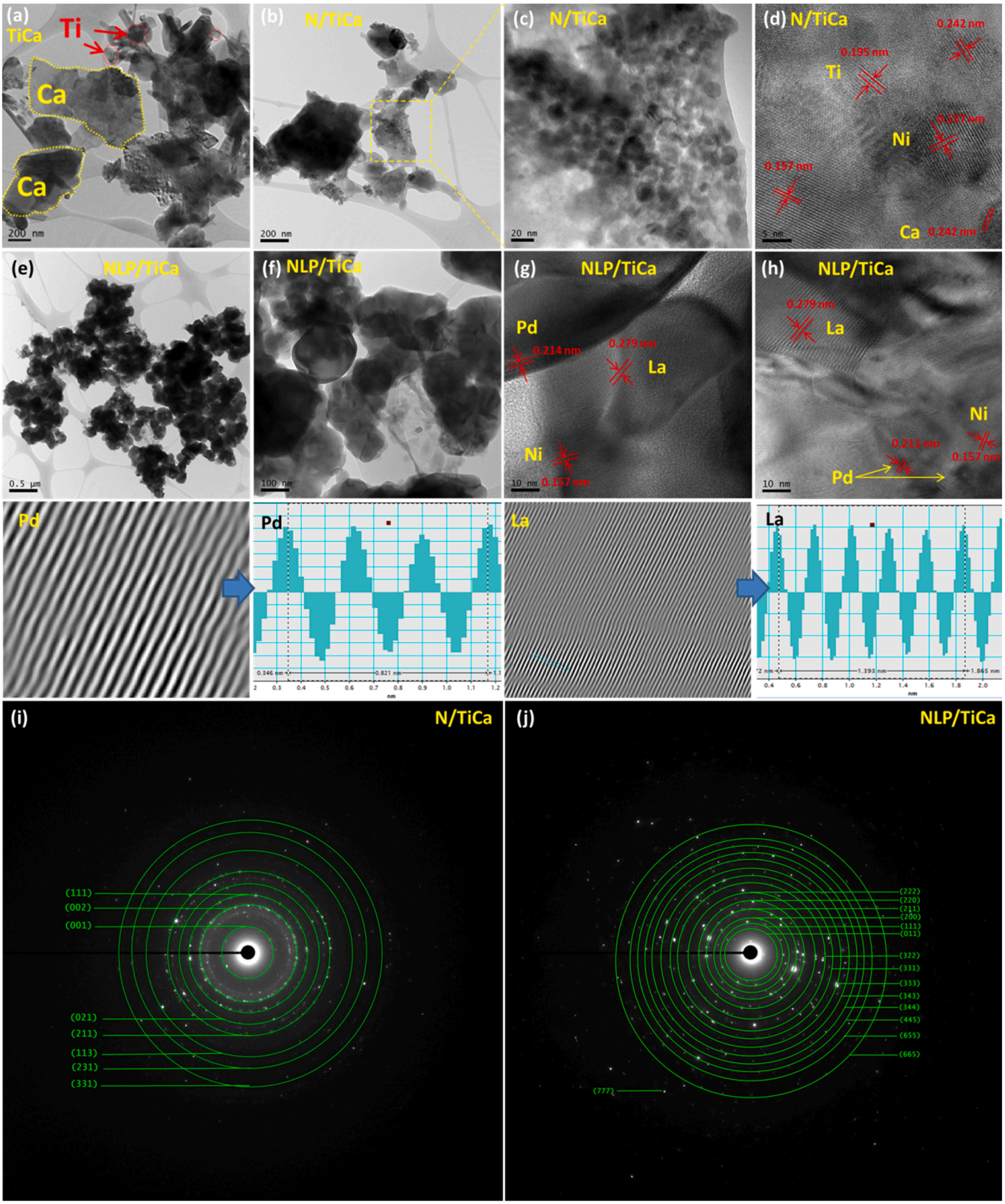

Fig. 4. TEM observations (a) TiCa, (b, c) N/TiCa, (e, f) NLP/TiCa, high-resolution TEM (HRTEM) images of (d) N/TiCa, (g, h) NLP/TiCa, SAED images of (i) N/TiCa, and (j) NLP/TiCa.

chemical contact, even though this impact of chemical interaction on catalytic activity is more often seen in Ni [25] and TiCa [31]. As in the case of the catalysts created by the deposition of Ni, La, and Pd on TiCa, strong bonding of deposited metals with the TiCa may promote efficient active center formation. In this regard, we conducted the H_2-TPR analysis to study the redox properties of as-prepared catalysts, and the quantitative and profile results are depicted in Table 1 and Fig. 3(b), respectively. H_2-TPR profiles of TiCa reveal that all the titanium-based oxides possess three reduction peaks at 268 °C, 411 °C, and 556 °C. These results differ from the H_2-TPR profiles of our previous research [31], most probably because we used organic ash as the source of calcium material. The low-temperature peak at about 268 °C was assigned to the reduction of surface oxygen species. TPR profile at 411 °C correlated with a partial reduction of TiO_2. The TPR curves for each sample show peaks over 500 °C, which are attributed to CaO reduction with significant TiO_2 interaction, leading to the creation of Ca (TiO_3) alloy, as demonstrated by XRD analysis. For the Ca sample, the peak seen at around 556 °C was connected to the process of $CaCO_3$, which is created by CaO carbonation, and decomposing. The peak at 556 °C for a mixed TiCa support might be due to a decrease in the oxygen covering the surface of CaO. With a wide shoulder up to 654 °C, the N/TiCa catalyst begins to reduce into Ni° species at 390 °C, showing a

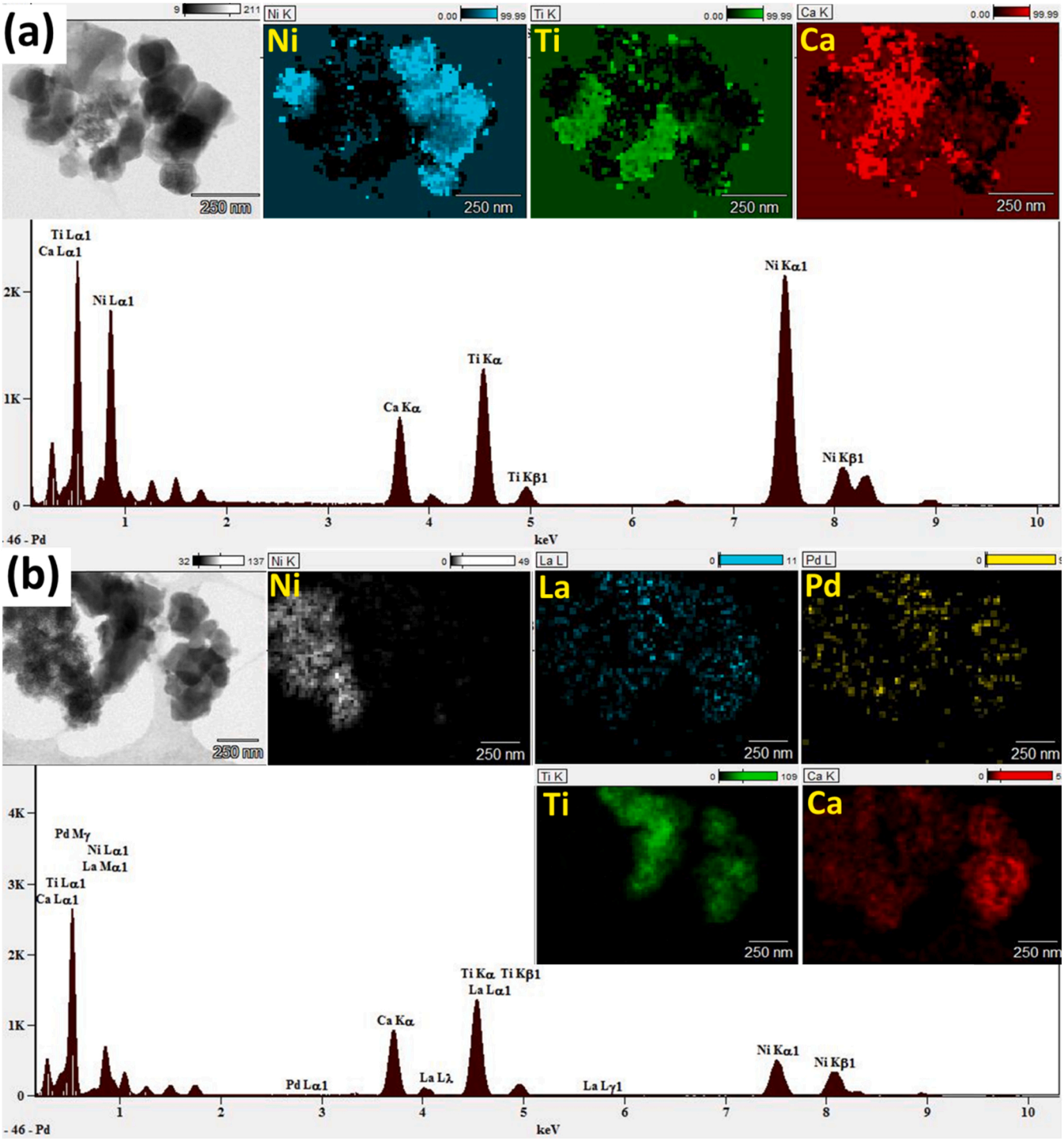

Fig. 5. EDX and Elemental mapping analysis of (a) N/TiCa, (b) NLP/TiCa nano catalysts.

low degree of reducibility and strong metal-support interaction with the TiCa. The reduction shoulder at 390 °C is associated with the reduction of nickel oxide ($NiO + H_2 \rightarrow Ni^{\circ} + H_2O$), which has poor interaction with the TiCa. This might be the reason for the H_2 consumption decreasing from 12.09 mmol/g to 9.53 mmol/g when Ni is introduced to the TiCa support. The second peak at 654 °C belongs to the reduction of the nickel aluminate ($Ni^{2+} \rightarrow Ni^{\circ}$) due to the significant interaction between the nickel and the TiCa. The two identified reduction processes have been labeled H_w (weakly adsorbed hydrogen) and H_s since they are characteristics of transition metals (strongly adsorbed hydrogen). For particles between 0.9 and 2.2 nm, Sayari et al. [50] 's correlation of a greater quantity of H_w is in excellent accord with the current results for N/TiCa, NL/TiCa, and NLP/TiCa samples. This can be due to the non-dissociative nature of the H_2 adsorption/desorption. N/TiCa, NL/TiCa, and NLP/TiCa samples, in contrast, have a high concentration of H_s species and metallic particles larger than 2.2 nm. This implies that Pd and La may facilitate H_2's dissociative adsorption. The former peak (418 °C) is ascribed to the reduction of La^{2+} to metallic Lanthanum (La°), and the latter peak at 677 °C is accredited to the reduction of Ni^{2+} to metallic nickel (Ni°), and the 677 °C peak consumes more H_2 than the 418 °C peak. Briefly, the low H_2 consumption peaks at 176 °C and 314 °C for the NLP/TiCa curve, corresponding to the total reduction of Pd^{2+} to Pd°. The addition of Pd retards the reducibility of the NL/TiCa, as it is demonstrated by the move of the maximum of the peak from 677 °C to 705 °C, therefore, that a Pd*La, La*Ni, La*Ti and Ca*Ti interaction exist as proven by XRD result for $LaPd_5$, $LaNi_5$, $La_{2.32}O_{12}Ti_4$, and $Ca(TiO_3)$ alloys, repectively.

The study of form, which includes shape, size, and structure, is known as morphology. Morphology is significant for studying nanostructured materials because, in this context, the form determines the physical and chemical characteristics. The morphologies of fresh catalyst were analyzed by TEM, HRTEM, and SEAD, as shown in Fig. 4, and the elemental composition of materials was identified by EDX and elemental mapping analysis, as shown in Fig. 5. The Gatan microscopy suite software version 2.11 was employed to analyze the materials' TEM and HRTEM images and lattice D-spacing. The morphology of the prepared samples is verified by TEM analysis. As revealed in Fig. 4(a), the precursor TiCa nanoparticles synthesized by the hydrothermal method are interconnected and overlapped, nano-sized irregular structures, and exhibit two different shapes of particles. The overlapping and interconnection of Ti and Ca elements might be because of the formation of TiCa alloys as confirmed by XRD analysis ($Ca(TiO_3)$ alloy) and discussed in the reducibility study. Ti is illustrated mainly in spherical nanoparticles with approximate sizes of 70 nm, while Ca particles are in irregular cubic and rectangular shapes with an average diameter of 300 nm with a lattice D-spacing of 0.195 and 0.242 nm, respectively. The HRTEM images also show lattice edges with a spacing of about 0.195 nm, matching the 101 crystal plane of anatase-type TiO_2 in the catalyst. As shown in the representative TEM images in Fig. 4(b) and (c), mesoporous nickel spheres with almost similar sizes and uniform spherical morphology were successfully synthesized. In the HRTEM image of Fig. 4(g) and (h), La has noticeable lattice spaces of 0.279 nm belonging to the (312) plane of $La_3Ni_2O_{6.84}$ orthorhombic structure, as confirmed by XRD. The lattice edges with spacing at 0.211 nm can be assigned to the (002) plane of $LaPd_5$ alloy, and the lattice edges value of 0.157 nm corresponds with the (211) plane of $LaNi_5$ alloy. The SEAD pattern further confirms this structure (Fig. 4(i) and Fig. 4(j)).

The elemental composition and the presence of Ni in N/TiCa (Fig. 5 (a)) and Ni, La, and Pd in NLP/TiCa (Fig. 5(b)) were confirmed from the EDX spectrum, which shows the presence of all the expected elements without having any external impurities. As seen in Fig. 5(a), metallic Ni particles are in close proximity to an amorphous TiCa phase. The EDX mapping of NLP/TiCa nanocatalysts (Fig. 5(b)) indicates despite its complexities with the existence of trace elements such as Pd, La, and Ni, it is not difficult to note that the dispersion effect of Ni, La, and Pd elements on the NLP/TiCa catalyst is better and more uniform. Pd metal particles have small particle sizes, do not aggregate and are typically evenly scattered. Compared with the N/TiCa monometallic catalyst, areas in which the colors of trimetallic catalyst mixed indicate the interface of the active metal due to their overlapping EDX signals. The elemental line scanning analysis of the NLP/TiCa further verified the strong interaction of metal support and the formation of alloys, which agrees with the XRD, TPR, and TEM analysis.

The catalytic activity of the catalyst surface and its resistance to carbon deposition in reforming and cracking processes are significantly influenced by its acid-base characteristics. The distribution of weak, intermediate, and strong basic sites and the total basicity of materials significantly impact the adsorption and dissociation capacity of the phenol and polymer molecules. This could speed up the removal of carbonaceous deposition from the catalyst surface, improving the catalytic performance and stability. Thus, CO_2-TPD and pyrrole probed IR spectroscopy was carried out on fresh catalysts to understand the influence of transition and noble metals NPs content on the basicity of TiCa catalyst. The results of CO_2 adsorption capacity and accessibility data of CO_2 uptake for the fresh catalysts are shown in Fig. 6. By measuring and fitting the CO_2 desorption peak, as shown in Table 1, it is possible to determine the catalyst's CO_2 desorption quantity. Fig. 6(a) shows that all catalysts display a broad desorption peak at various temperatures, demonstrating the presence of several types of basic sites in the catalysts, including weak basic sites (100–230 °C), moderate basic

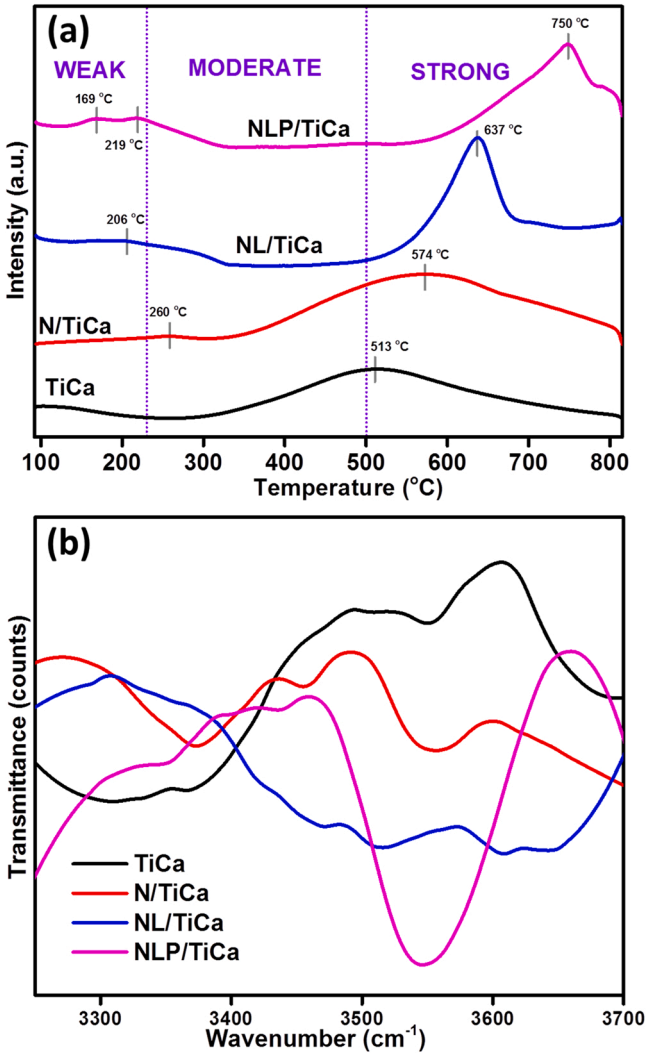

Fig. 6. (a) Temperature-programmed desorption of CO_2 (CO_2-TPD) and (b) Pyrrole adsorbed FTIR spectra curves of the fresh catalysts.

sites (230–500 °C), and strong basic sites (above 500 °C) [51]. While the C atom in CO_2 is the electron-deficient core and the CO_2 molecules have vacant orbitals at low energy levels, TiCa may readily shed its outside electrons due to its relatively low initial ionization energy [52]. Many basic sites and adsorbed O2 on the surface were attributed to the diminished catalysts' capacity to absorb CO_2. The medium desorption peak at 260 °C for the N/TiCa nanocatalyst is because of the under-coordinated O^{2-}. The NL/TiCa, and NLP/TiCa nanocatalysts detected small shoulders at around 169, 206, and 219 °C are assigned to surface –OH [53] indicating the presence of small weak basic sites resulting in less desorption and activation of CO_2 in their structure. Those desorption peaks corresponded to the interaction of CO_2 with weakly basic hydroxyl groups on NL/TiCa, and NLP/TiCa nanocatalysts. Furthermore, adding La and Pd materials produced higher peaks in regions 637 °C and 850 °C; thus, it is indicated that adding La and Pd materials leads to the higher CO_2 adsorption capacity of the catalysts. The peak position given to the strong basic increased further after Pd loading, indicating its strongest binding affinity to CO_2 that enhanced the catalyst's basicity. This inference was made because Pd and La interactions with the N/TiCa nanocatalysts are compatible with the observed increase in the quantity of CO_2 desorbed. Since CO_2 molecules may be converted into reactive $CO_2^{\delta-}$ species as a result of the transition and noble metals utilized in this study, it is possible to efficiently boost CO_2 molecule absorption by the N/TiCa, NL/TiCa, and NLP/TiCa nanocatalysts. As increased basicity may decrease the production of coke [54] during the reaction, it is anticipated that the change of basicity with La and Pd concentration in the catalysts may have some impact on the catalytic activity. The H_2-TPD, in which NLP/TiCa exhibits substantial H_2 adsorption, and the CO_2-TPD exhibit strong correlations.

The catalyst's basic sites engage with the pyrrole's N − H group via the development of an H−bond interaction, which the stretching can see in the N − H group. Fig. 6(b) shows the measurement of adsorbed pyrrole on the calcined catalysts using N − H stretching and the wide peak in the range of 3200–3700 cm^{-1}. Additionally, it has been shown that pyrrole chemisorbs dissociatively over powerful basic metal oxides and that deprotonation of pyrrole on the most powerful basic oxygens results in the generation of pyrrolate anions that are stabilized by surface cations [55]. In N/TiCa and NLP/TiCa nanocatalysts, a strong peak was found at ~3544 cm^{-1}, indicative of stretching vibrations between the H atom of pyrrole and the (≡Ni−O^- and ≡Pd−O^-) group of basic oxygen present in the catalysts' framework. Interestingly, the NLP/TiCa catalyst had a larger peak intensity than the other catalysts, indicating that the catalyst was constructed with many basic sites. The development of intra- and inter-particle porosity was one potential factor that increased the basicity of the NLP/TiCa catalyst [56]. The peak above 3544 cm^{-1} also represented the N − H group of pyrrole molecules in the environment, and the N − H band (physisorbed pyrrole in a liquid-like state) interacts with the π-system of nearby pyrrole molecules.

Metal-acid bifunctional compositions are often used in industrial catalysts for cracking and reforming processes, where metallic sites catalyze hydrogenation/dehydrogenation reactions, and acidic sites catalyze cracking. One of the crucial variables affecting the catalytic performance in the n-situ pyrolysis-catalytic steam reforming processes is the catalyst's acidity. The findings of NH_3-TPD's analysis of surface acidity in terms of the quantity and strength of acid sites are shown in Fig. 7(a) and Table 1. All samples have strong acid sites because they showed the presence of peaks above 400 °C. The highest quantity and strength of acid sites for the TiCa sample proposes that the superior acidity of the TiCa nano-catalyst may be due to the Brønsted acid sites on the catalyst [31]. A higher acidity may cause to produce better activities, as it is known to break C−C and CO− binding, but it may also favor higher coke formation during the reforming reactions. Therefore, the bare TiCa might face catalytic deactivation by coke deposition. As can be seen in the quantitative data, N/TiCa and NL/TiCa had basically similar desorption of NH_3, indicating that each sample's total acid site density was the same. Ni and La were added to the TiCa structure, which

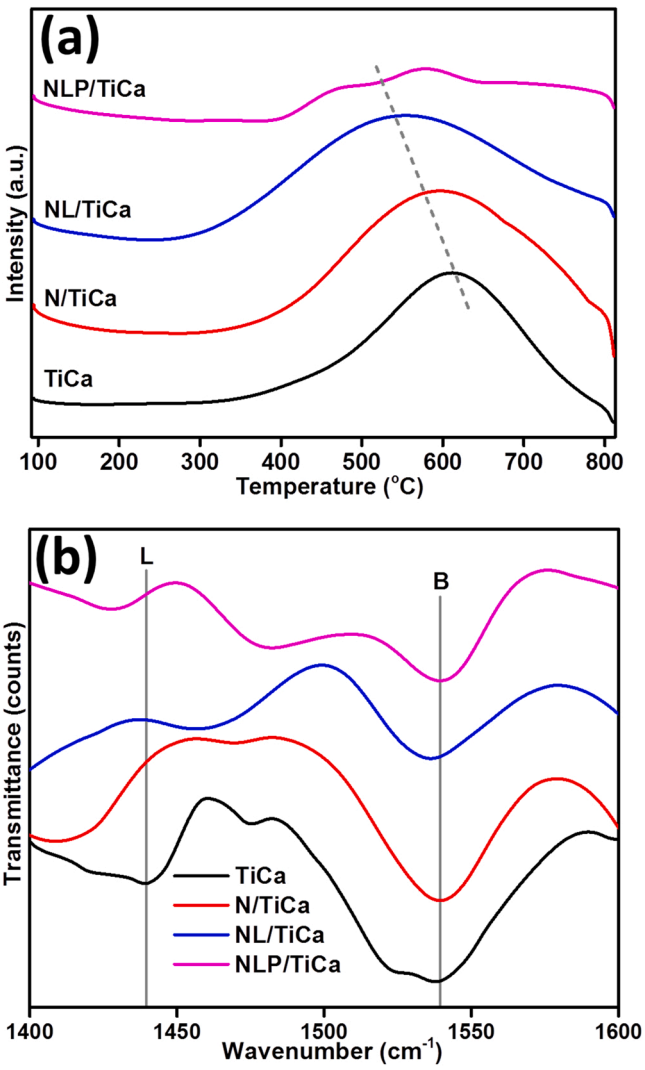

Fig. 7. (a) Temperature-programmed desorption of ammonia (NH_3-TPD) and (b) Pyridine-FTIR spectra of the fresh catalysts.

reduced the number of acid sites while simultaneously shifting the high-temperature peak to lower temperatures. With Ni and La in porous TiCa support, Ni and La and support atoms are bonded to form Lewis acid sites due to the different electronegativity between the transition metals and the TiCa atoms. Thus, the acidic sites in N/TiCa and NL/TiCa may be formed by the sites containing electron holes in porous TiCa. These two catalysts had mild acid and basic properties compared to the bare TiCa with the strongest acidity and NLP/TiCa with the strongest basicity. The low acido-basicity properties of N/TiCa and NL/TiCa might also be attributed to the low amount of alkali, which was insufficient to form strong interactions between the alkali and the TiCa support during the preparation of catalysts. Since the –OH groups were lost when Pd^{2+} ions interacted with the support surface after the addition of Pd metal, it is possible that the catalyst's acidic quantity was dramatically reduced with the insertion of Pd atoms [57]. Consistent with the results of Pd-modified NL/TiCa, the introduction of Pd leads to catalysts of higher basicity and lower acid site having bifunctional properties, which are significant in the in-situ catalytic steam reforming of phenol coupled with thermal cracking (or pyrolysis) of cellulose.

The distribution and nature of acidic sites and their effect on selectivity must also be considered. As a consequence, the acidity of the catalysts was further investigated using FTIR spectroscopy with adsorbed pyridine as a probe molecule, and the results are shown in Fig. 7(b). For coordinatively bound (Lewis acid sites, "L") and protonated bonded

(Brønsted acid sites, "B") pyridines, the bands at 1540 and 1440 cm^{-1} were used as measures, respectively [58]. Higher wavenumbers also demonstrated better surface adhesion, increasing Brønsted acid's strength. It is noteworthy that the TiCa has many Brønsted and Lewis acid sites compared to other catalysts with transition and noble metals. All samples had bands at around 1540 cm^{-1} caused by pyridine adsorbed on Brønsted acid sites; however, the N/TiCa and NL/TiCa catalysts did not show any bands at 1440 cm^{-1} that were caused by the pyridinium ion (PyH^{+}), which is responsible for Lewis acid sites. This does not imply that there are no Lewis acid sites; it only indicates that the Lewis acid sites were insufficiently powerful to create the pyridinium ion. However, it is simple to induce carbon deposition and deactivate the catalyst at the Brønsted acid and strong acid sites [59]. The Pd NPs inserted into an NL/TiCa have jointly disturbed the catalyst's Brønsted and Lewis acid phases. As Pd addition increases, the catalysts' pyridine adsorption peaks become less intense, indicating a weaker acid. To conclude, reducing the strength of Brønsted and Lewis acid phases is vital to prevent the undesired reaction, especially for the reactions that deal with polymer molecule thermal cracking. Therefore, it is expected that NLP/TiCa will show high catalytic activity and selectivity in the in-situ catalytic steam reforming of phenol coupled with the pyrolysis of cellulose.

The spectroscopic method known as FTIR is highly effective and widely used for identifying functional groups in compounds and complex substances. In this work, KBr pellets are utilized as a carrier for the sample in the IR spectrum since they are optically transparent to light in the IR measurement range. We choose the KBr pellet approach for FTIR spectroscopy because it is straightforward and enables us to run the whole mid-IR region down to 400 wavenumbers without running split mulls [60]. All catalysts were subjected to FTIR-KBr spectroscopy, and the spectra in the 4000–400 cm^{-1} region are shown in Fig. 8. The TiCa sample exhibited an absorption peak at 957 cm^{-1}, ascribed to C–O symmetrical structure ether groups. These lines are connected to chromophore vibrations (C═C stretches and hydrogen out-of-plane vibrations, respectively), so it is more likely that exchangeable protons will influence them in the chromophore than exchangeable protons in other regions of the molecules. This peak shifted to 833 cm^{-1} after adding Ni, La, and Pd metals. The stretching vibrations of metal oxide in octahedral group complex Ni(III)–O^{2-}, La(III)–O^{2-}, and Pd(III)–O^{2-} tetrahedral group complex formation is proved by the bands at 594 cm^{-1}. The FTIR spectra at 1165 cm^{-1} and 1774 cm^{-1} for the N/TiCa, NL/TiCa, and NLP/TiCa nanocatalysts correspond to the stretching and bending vibration of C−H, C−O−H, C−O−C bonds and –C═O absorption vibration, respectively. There is a highly characteristic weak band at 2376 cm^{-1} for all samples that correspond to vibrations of the υ(C−H) mode related to CH_2 −CO groups; while the peak at 2932 cm^{-1} indicates the existence of C−H vibrations in methyl (–CH_3) and methylene (−CH_2 −) group. The ν(OH) band around 3642 cm^{-1}, which is assigned to non-hydrogen-bonded water molecules coadsorbed with CO, exhibits a gradual decrease by adding Ni, La, and Pd metals. Besides, FTIR bands observed in the hydroxyl region at 3765 cm^{-1} are ascribed to the vibration of OH– groups adsorbed along the support surface and correspond to terminal hydroxyl groups. The biggest bands centered at 1443 cm^{-1} can be attributed to the surface complex of –CH_2 bending (methylene group), while the 1463 cm^{-1} peak can correspond to the presence of metal carbonates (stretching vibration of C═C). Notably, the intensity of FTIR peaks ascribed to the methylene groups and metal carbonates of the NLP/TiCa, NL/TiCa, and N/TiCa catalysts were more intense than the TiCa catalyst. This suggests that the differences in the surface methylene groups are caused by the Ni, La, and Pd crystal structure.

3.2. Catalytic performance test

The catalyst's performance on hydrogen generation and its stability in the system have been investigated using catalytic activity parameters regarding phenol conversion, product yield, temperature (for the best catalyst), and time on stream performance. The screening of reduced catalysts was performed at 600 °C. The activity was investigated and repeated for six cycles with an experimental duration lasting 60 min for each run; the results are illustrated in Fig. 9. Analysis of produced gas composition shows that the most significant changes in concentration occur for H_2 yield, CO_2 yield, and phenol conversion. It was confirmed that the addition of transmission and noble metals did not significantly affect CO yield but slightly decreased. At TiCa nanocatalyst, the phenol conversion and H_2 yields were 34.3% and 40.5%, respectively. Phenol conversion was increased to 49.3% and 70.2%, and H_2 yield enhanced to 45% and 57.2% for the N/TiCa and NL/TiCa, respectively. The highest conversions of phenol at 82.6% and H_2 yield at 82.2% were achieved with NLP/TiCa catalyst. The increased catalytic activity under the NLP/TiCa nanocatalyst can be attributed to the increased surface area, metal support interaction, basicity, and active metal distribution of the synthesized catalyst as characterized by BET surface area, CO_2-TPD, H_2-TPR, and EDX. A reactant's contact with a higher surface area affects the number of collisions and the reaction rate. The NLP/TiCa nano catalyst has more porosity and is more active than those other samples because it has more surface area to form the active sites, leading to greater

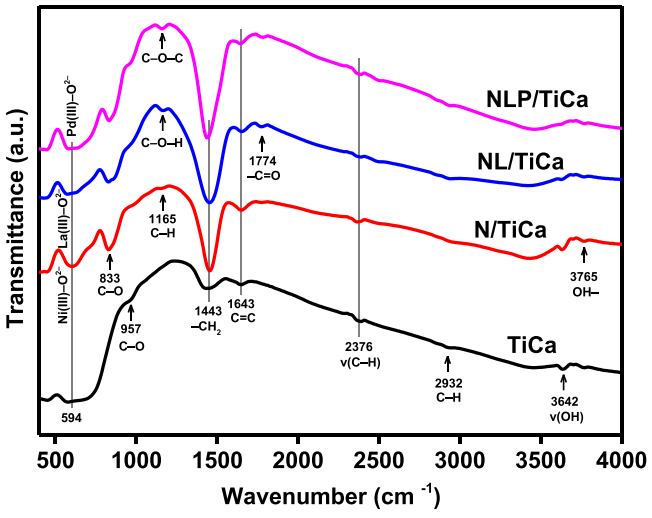

Fig. 8. Fourier transform infrared (FTIR-KBr) profiles of the fresh catalysts.

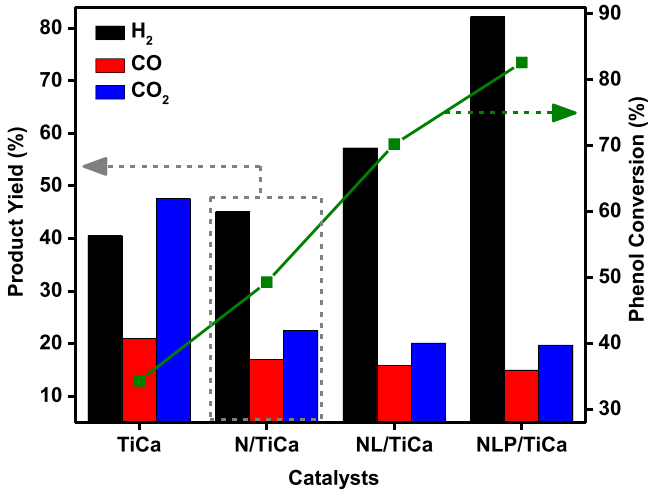

Fig. 9. Catalytic evaluation of different nanocatalysts in flow reactors. Reaction conditions: (catalyst: 0.25 g, pressure: 1 atm, reaction temperature: 600 °C, feed (cellulose-phenol mixture) to water volume ratio of 1:9).

activities in this work. As a result of the large dispersion of active sites and the accessibility of reactants to active sites, we can assert that the high BET surface area and pore volume of Pd-containing catalysts increase the selectivity to hydrogen. Furthermore, the maximum hydrogen consumption of the NLP/TiCa nanocatalyst in the H_2-TPR process also proves the total reduction of Pd^{2+} to Pd°. The addition of Pd in the NL/TiCa increased the reducibility properties of the catalyst; therefore, a Ca*Ti, Pd*La, La*Ti, and La*Ni interaction exist as proven by XRD result for $LaPd_5$, $LaNi_5$, $La_{2.32}O_{12}Ti_4$, and $Ca(TiO_3)$ alloys. From the particle size distribution of the active metal in the EDX images, it can also be found that the NLP/TiCa nanocatalyst has a smaller particle size and a more uniform distribution. Therefore, it shows the most excellent catalytic activity in the reaction. According to the CO_2-TPD and Pyrrole adsorption FTIR spectra findings in Fig. 6, the NLP/TiCa nanocatalyst's more excellent catalytic activity may be caused by the nature of Pd and the existence of a significant number of basic sites in the structure [61]. These findings suggest that the catalyst's basicity facilitates the considerable adsorption of CO_2 molecules and increases H_2 production. For instance, Pizzolitto et al. [62] observed that the NiLa/ZrO_2 catalyst's basicity increase significantly reduced the dehydration of ethanol. We also found the same positive effect of basic catalyst sites on the catalytic pyrolysis steam reforming reaction PET-phenol for H_2 generation [25,27,35,45]. Less crystal size of NLP/TiCa nanocatalyst (as seen in XRD analysis) plays a substantial part in minimizing the coke production and deposition and enhancing the catalyst lifetime throughout the in-situ pyrolysis-catalytic steam reforming reaction process. Given its good catalytic performance for phenol steam reforming (in terms of phenol conversion and H_2 selectivity), the NLP/TiCa nanocatalyst was selected for further evaluation based on temperature effect and deactivation check studies.

The reforming temperature significantly influences the concentration of reforming products; the results are shown in Fig. 10. Conversely, using only 500 °C resulted in 67.6% of phenol conversion and 59.2% of H_2 yield. Due to the accelerated phenol steam reforming reaction ($C_6H_5OH + 11H_2O \leftrightarrow 6CO_2 + 14H_2$) and water gas shift reaction ($CO + H_2O \leftrightarrow CO_2 + H_2$), an increase in temperature regulates the enhancement of phenol conversion into gaseous products and H_2 yield. Higher gas yields compared to 500 °C were seen along with the high conversion at the maximum temperature, which is anticipated given that the gas-forming cracking processes are thermally regulated. Almost complete conversion of phenol (98.7%) and maximum H_2 yield (99.6%) were achieved at 800 °C. At the same time, the CO_2 yield is enhanced from 16.7% at 500 °C to 27.4% at 800 °C, while the CO yield decreases from 18.9% to 8.8% due to improving reaction conditions for water gas shift reaction. In addition, it was also observed that the increase in acid sites, decrease of the surface area, and metal dispersion of the TiCa nanocatalyst were sufficient to justify the low phenol conversion and H_2 yield. This made it feasible to conclude that the major pathway for the deactivation of the TiCa catalyst and likely has an impact on how well the TiCa catalyst performs in terms of producing H_2 is the development of amorphous coke. This statement is verified in the characterization of used catalysts.

The phenol conversion and H_2 production over the NLP/TiCa nano catalyst were evaluated at 600 °C for 72 h of time-on-steam, and the stability results are displayed in Fig. 11. With a slight decrease (~4% loss in yield), the H_2 yield was maintained constantly at approximately all reaction times. During the reaction, the CO yield decreased from 14.9% to 8.6%, while the CO_2 yield fraction increased from 19.7% to 23.7%. After 32 h, it was noticeable that phenol conversion was about 74% and remained almost stable (with a negligible decrease) for the rest of the time (72.3% at 72 h). This is almost in agreement with the total basic sites, Pd and La dispersion, high metal-support interactions, and different alloys determined by CO_2-TPD, H_2-TPR, and XRD, respectively.

3.3. Liquid products composition

To understand the component presented in the produced liquid during the thermal reaction of cellulose and steam reforming reaction of phenol, the liquid product at 600 °C was analyzed by GCMS technique, and the identified compounds are summarized in Table 2. The chemical components in the liquid product are analyzed in accordance with the thermal breakdown of the feedstock's cellulose and phenol. Due to their volatility and complicated structure, several chemicals were undetected. The aromatics and alkanes occupied mostly the liquid product, mainly from cellulose decomposition. The liquid was mainly composed of C_2-C_{12} aliphatic hydrocarbon, C_6-C_9 aromatic hydrocarbon, C_{13}-C_{18} aliphatic hydrocarbon, and C_{19}-C_{72} aromatic hydrocarbon. At a retention time of ~59 min, the liquid was composed of a C_{70} aliphatic hydrocarbon for the NL/TiCa nanocatalyst. It is evident that despite the variable catalytic activity of different catalysts, the relative product profile remains largely the same, with 1-propanol, ethanol, toluene, and phenol (incoverted reactant) being the major product for all the catalysts except 2,4-dimethyl-benzo[*h*]quinoline, and hexadecane components for the N/TiCa catalyst. The aromatic byproducts of the cracking process, which resulted from breaking the main chain in cellulose and dehydration of the –OH bond on its alkyl chains, may also be the source of phenolic compounds. The chemicals contain oxygen such as $C_8H_{10}O_5PW^+$, $C_{40}H_{48}O_4$, $C_{29}H_{23}NO$, C_4H_7OH, $C_{14}H_{42}O_7Si_7$, $C_{16}H_{32}$, $C_{17}H_{34}O_2$, $C_{23}H_{39}NO_2S$, $C_{28}H_{43}NO_2$, $C_{28}H_{45}NO_2$, $C_{40}H_{73}NO_5Si_4$, and

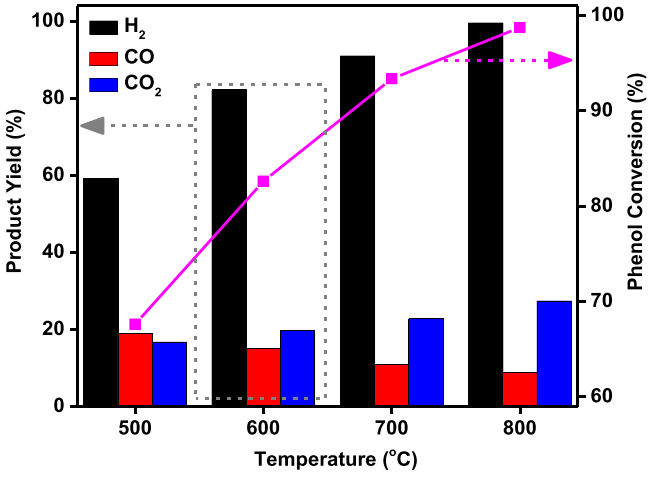

Fig. 10. Effect of reaction temperature on gaseous product yield and phenol conversion. Reaction conditions: NLP/TiCa catalyst: 0.25 g, pressure: 1 atm, feed (cellulose -phenol mixture) to water volume ratio of 1:9.

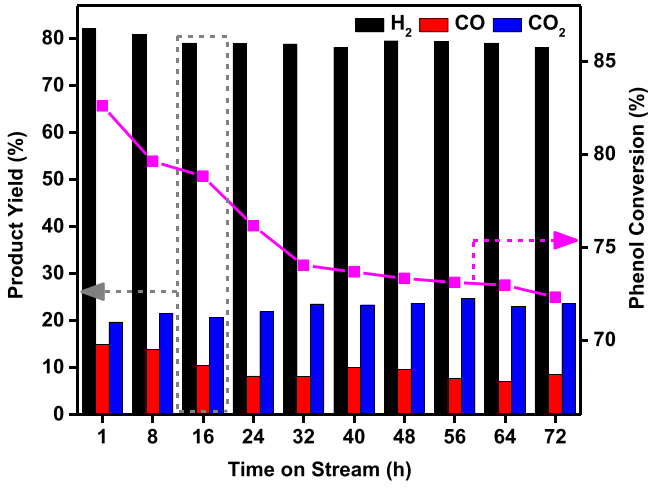

Fig. 11. Effect of time-on-stream on H_2 production and phenol conversion over NLP/TiCa nanocatalyst at the temperature of 600 °C.

Table 2
Constitution of liquid products after the reactions at 600 °C.

Compound	Molecular Formula	TiCa	N/TiCa	NL/TiCa	NLP/TiCa
(E)− 2-bromobutyloxychalcone	$C_{19}H_{19}BrO_2$	0	0	0	0.35
.pi.-Pentamethylcyclopentadienyl-trichlorogermyl-ethylisonitril-carbonyl-trimethylphosphan-tungsten	$C_8H_{10}O_5PW^+$	1.01	0	0	0
.beta.,.epsilon.-Carotene-3,3′,8,19-tetrol, 7,8-dihydro-	$C_{40}H_{56}O_2$	0	0	0	1.35
1 H-Indole, 1-methyl-2-phenyl-	$C_{15}H_{13}N$	0	0	0.35	0
1,3,5-Cycloheptatriene	C_7H_8	1.34	0.27	0	0
1,5-benzodiazocin-6(1 H)-one, 8,10-bis(dodecylsulfonyl)− 2,3,4,5-tetrahydro-5-methyl-	$C_{35}H_{62}N_2O_5S_2$	0	0	0	0.75
1-Propanol	C_3H_8O	0.68	1.26	2.22	0.55
1-Propanol, 2-methyl-	$C_4H_{10}O$	0	0	0	0.22
2,2′-Bi[1,3,5,2,4,6-triazatriphosphorinyl],2,2′-dibutyl-4,4,6,6,4′,4′,6′,6′-octachloro-	$C_{38}H_{42}I_2N_2S_2$	0	0	0.41	0
2,3-Epoxybutane	C_4H_8O	0	0	0	0.28
2,4,6-Cycloheptatrien-1-one, 3,5-bis-trimethylsilyl-	$C_{13}H_{22}OSi_2$	0	0	0.31	0
2,4,6,8,10,12-Tridecahexaenoic acid, 13-(3-chloro-4-methoxyphenyl)-, 2-decyl-3-methoxy-5-pentylphenyl ester	$C_{42}H_{55}ClO_4$	0	0	0	4.72
2,5-Cyclohexadien-1-one, 3,3′-(3,7,11,15-tetramethyl-1,3,5,7,9,11,13,15,17-octadecanonaene-1,18-diyl)bis[6-hydroxy-2,4,4-trimethyl-	$C_{40}H_{48}O_4$	0.57	0	0	0
2-Ethylacridine	$C_{15}H_{13}N$	0	0	0	0.29
4-(3-Fluoro-phenyl)− 9-methyl-2-trifluoromethyl-2 H-pyrido[1,2-*a*][1,3,5]triazine-2-carboxylic acid methyl ester	$C_{17}H_{13}F_4N_3O_2$	0.76	0	0	0
5,10-Di[4-(1-Acetamidomethyladamantyl-3)− 3-methoxyphenyl]− 15,20-di(4-methoxyphenyl)− 21 H,23 H-porphine	$C_{74}H_{76}N_6O_6$	0	0	0.58	0
5-(p-Aminophenyl)− 4-(4-biphenylyl)− 2-thiazolamine	$C_{16}H_{15}N_3S$	0.53	0	0	0
5-Imino-1,4,4-triphenyl-2-imidazolinethione	$C_{21}H_{17}N_3S$	0	0	0.64	0
5-Methyl-2-phenylindolizine	$C_{15}H_{13}N$	0.61	0	0	0
Anthracene, 9,10-diethyl-9,10-dihydro-	$C_{18}H_{20}$	0	0	0.46	0
Benzeneethanamine, 5-benzyloxy-3-fluoro-.beta.-hydroxy-N-methyl-	$C_9H_{12}FNO_2$	0	0	0	1.25
Benzo[*h*]quinoline, 2,4-dimethyl-	$C_{15}H_{13}N$	0.59	0	1.43	0.39
benzoic acid, 4-fluoro-3-nitro-, 2,4-bis(1,1-dimethylpropyl)phenyl ester	$C_{29}H_{23}NO$	0.26	0	0	0
Cyclobutanol	C_4H_7OH	0.84	0	0	0
Cycloheptasiloxane, tetradecamethyl-	$C_{14}H_{42}O_7Si_7$	0.19	0	0	0
Cyclohexadecane	$C_{16}H_{32}$	0.3	0	0	0
Cyclotrisiloxane, hexamethyl-	$C_6H_{18}O_3Si_3$	2.27	0.71	0	0
Dasycarpidan-1-one	$C_{17}H_{20}N_2O$	0.39	0	0	0
Demeclocycline	$C_{21}H_{22}Cl_2N_2O_8$	1.1	0	0	0
Eicosane	$C_{20}H_{42}$	0.38	0	0	0
Ethane, 1-trimethylsilyl-2-[bis(trifluoromethyl)boryl] methylmethyleneimine(N-B)-	$C_9H_{16}BF_6NSi$	0.4	0	0	0
Ethanol	CH_3CH_2OH	41.89	78.4	55.63	67.7
Ethyl Acetate	$CH_3COOC_2H_5$	0.6	1.44	0	0
Hexadecane	$C_{16}H_{34}$	1.57	0	0.49	1.12
Hexestrol, 2TMS	$C_{24}H_{38}O_2Si_2$	0	0	0.56	0
Lanost-9(11)-en-18-oic acid, 23-(acetyloxy)− 3-[(4-bromobenzoyl)oxy]− 20-hydroxy-,.gamma.-lactone, (3.beta.,20.xi.)-	$C_{39}H_{53}BrO_6$	0	0	0	0.56
Phenol	C_6H_5OH	25.96	17.36	23.92	20.31
Picolinyl 12-methyltridecanoate	$C_{17}H_{34}O_2$	0.79	0	0	0
Picolinyl 2-thia-stearate	$C_{23}H_{39}NO_2S$	0.44	0	0	0
Picolinyl 7,13,16-docosatrienoate	$C_{28}H_{43}NO_2$	4.34	0	0	0
Picolinyl 7,13-docosadienoate	$C_{28}H_{45}NO_2$	2.38	0	0	0
Pregnan-20-one, 3,11,17,21-tetrakis[(trimethylsilyl)oxy]-, o-(phenylmethyl)oxime, (3.alpha.,5.beta.,11.beta.)-	$C_{40}H_{73}NO_5Si_4$	2.51	0	0	0
Silane, dimethyl-	C_2H_6Si	0.86	0	0	0
Silane, dimethylisobutoxypentadecyloxy-	$C_{21}H_{46}O_2Si$	0.43	0	0	0
Toluene	C_7H_8	5.09	0.56	0.81	0.15
Triethylamine	$C_6H_{15}N$	0	0	12.21	0
urea, N,N′-bis(2-mercaptoethyl)-	$C_5H_{12}N_2OS_2$	0.91	0	0	0
SUM		**100**	**100**	**100**	**100**

$C_{21}H_{46}O_2Si$ produced for the TiCa nanocatalyst could lead to the instability of catalyst. The oxygen compounds in produced fuel decreased with the addition of transition and noble metals NPs deposited on TiCa, indicating that Ni, La, and Pd metals promoted deoxygenation, and more oxygen compounds were decomposed into low molecular-weight substances. The occurrence of 2,4-dimethyl-benzo[*h*]quinoline is the unique structure of petroleum triaromatic azaarenes that could be more firmly established after the identification of individual compounds. It has been possible to radiolabel exosomes, hydrogels, and other biological materials since 1982 with the help of the generated hexadecane chemical. This substance is also helpful for positron emission tomography. Catalytic cracking activity of the cellulose and phenol under NLP-TiCa catalyst produced unique compounds such as (E)− 2-bromobutyloxychalcone, beta,epsilon-Carotene-3,3′,8,19-tetrol, 7,8-dihydro-, 1,5-benzodiazocin-6(1 H)-one, 8,10-bis(dodecylsulfonyl)− 2,3,4,5-tetrahydro-5-methyl-, 2,4,6,8,10,12-Tridecahexaenoic acid, 13-(3-chloro-4-methoxyphenyl)-, 2-decyl-3-methoxy-5-pentylphenyl ester and Lanost-9(11)-en-18-oic acid, 23-(acetyloxy)− 3-[(4-bromobenzoyl)oxy]− 20-hydroxy-,.gamma.-lactone, (3.beta.,20.xi.). The Pd metal induced stronger cracking activity than other catalysts by significantly increasing the proportion of aromatics while significantly decreasing the oxygenated products (including phenols). Furthermore, it has been shown that the H_2 yield and phenol conversion during the catalytic process seem to have increased in the presence of the NLP/TiCa catalyst (see Fig. 9). The liquid products were further analyzed using the FTIR technique.

The FTIR method was used to identify the functional groups present in the liquid fuel, and the FTIR curves with the intensities of each band are displayed in Fig. 12 (a) and Fig. 12 (b). The absorption band present in the wave number range 632 cm^{-1} can be linked to the OH– vibration [63]. At band detection 879 cm^{-1} (HNO_3), the carbonate bending mode can be assigned to the out-of-plane deformation band [64]. There is a substantial boost in intensity of the bands at about 1033 cm^{-1}

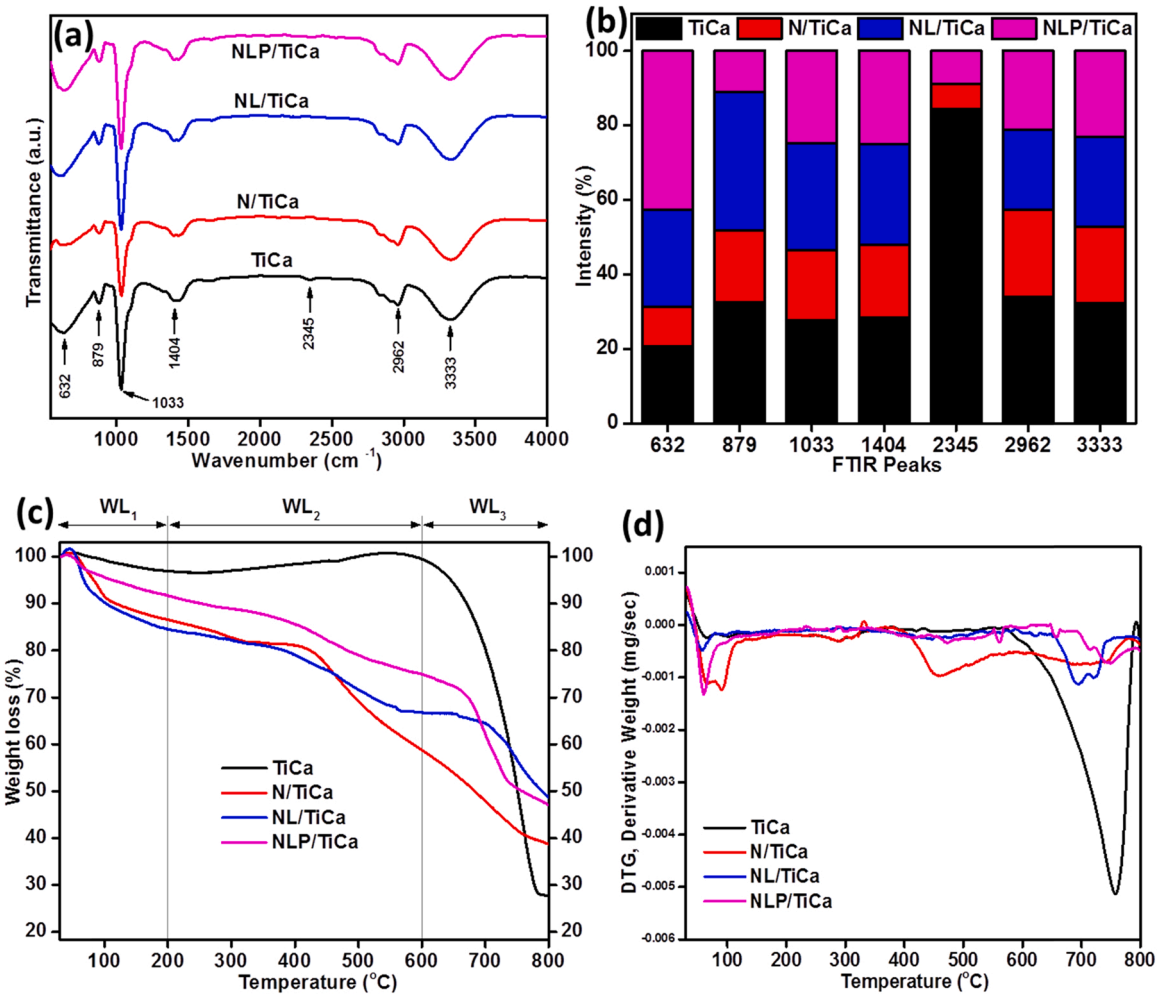

Fig. 12. (a) FTIR spectrum of pyrolysis liquid products for all catalysts with (b) the condensation of bands strengths; (c) TGA curves (d) DTG profiles of used catalysts.

wavelengths, signifying the chemical functional groups of $–CH_2–$ bending vibration of the aliphatic hydrocarbon [65]. Andrea et al. [66] stated that the bands at 1033 cm^{-1} could also be attributed to the C–H in-plane deformation vibration of 1,4-disubstituted or 1,2,4-trisubstituted benzene rings. This peak might also correspond to the C–O stretching and C–O bending of the C–O–H carbohydrates [67]. The band at 1404 cm^{-1} signified carboxylate C═O stretching weakened, demonstrating that the non-conjugate C═O structure in lignin has been decomposed [68]. This peak may also be ascribed to the aliphatic C−H deformation of CH_2 and CH_3 bending and C−OH deformation of COOH, COO^- symmetric stretch [69]. The characteristic absorption peak at 2345 cm^{-1} corresponds to CO_2 based on its vibrational occurrence and reflection as a 1,3,5-triamino-2,4,6-trinitrobenzene thermal decomposition product [70] and the O–C–O anti-symmetric stretching mode [71]. The vibration peaks of $-CH_3$ ($\nu_{as}(CH_3)$) in 2,5-dimethylfuran were observed at 2962 cm^{-1} [72,73], and symmetric and asymmetric stretching vibration of N − H (ν(NH) bound) [74,75] and the presence of urethane groups [76,77] were observed at 3333 cm^{-1}.

3.4. Post-reaction characterization

Characterization of the spent catalyst is critical for stabilizing stable catalysts against coke formation and long-term usage. The transient deactivation of the catalyst caused by the buildup of carbonaceous deposits (coke) during catalysis affects throughput, necessitates regeneration procedures, and results in a partial permanent loss of catalytic efficiency. This part analyzed the spent catalysts by TGA-DTG, CHNS, BET FTIR-KBr, and TEM. By observing the weight change that occurs while a sample is heated at a consistent rate, the TGA analytical method may be used to evaluate a material's thermal stability and the percentage of volatile components. The rates at which these volatile components are removed in %/min are determined by DTG, and results are shown in Fig. 12 (c) and Fig. 12 (d) and Table 3. The TGA curves of the used catalysts may be roughly separated into three sections, as observed. Weight loss in the first stage, denoted by WL_1, is evident in the temperature range of 25–200 °C and results from removing adsorbed water and unreacted molecules. The chemical adsorbed on the sample's surface or found in the mesopores is responsible for the WL_1 [78]. The second part (WL_2), located in the medium temperature range (200–600 °C) shows an increasing tendency in weight percent and can be attributed to the burning of deposited coke. Here as "coke," we considered the carbon deposited on the catalyst and all the condensed hydrocarbons determined by the material balance. The inadequate breakdown of nitrate during the creation of metal oxides should also contribute to the WL_2. The WL_2 area is ascribed to the overlaps of metal oxidation and removal of the amorphous carbon, except for the weight increase of the TiCa catalyst, which may be driven by the oxidation of the metallic Ti and Ca [10,16]. Amorphous carbon burns at temperatures lower than 400 °C [79–81]. Amorphous carbon may be readily removed by oxidizing at low temperatures, but it often encircles the catalyst's active metal particles and renders it inactive. The third phase (WL_3) above about 600 °C comprised the decomposition of remaining

Table 3
Weight losses, carbon substances, and surface area of the spent samples.

Catalysts	Weight loss (%)			Total weight loss (%)	Carbon Content (wt%)[a]	Fresh catalyst S_{BET} (m^2/g)	Spent catalyst S_{BET} (m^2/g)[b]	V_p (cm^3/g)[c]	D_p (nm)[d]	Difference between S_{BET} (a-b)
	WL_1	WL_2	WL_3							
TiCa	3.09	-2.55	71.77	72.31	13.80	6.26	0.131	0.0068	208.43	6.131
N/TiCa	13.46	27.80	20.10	61.36	9.60	11.89	1.390	0.0105	30.22	10.498
NL/TiCa	8.37	16.67	27.94	52.98	4.10	18.01	3.890	0.0205	21.08	14.115
NLP/TiCa	15.48	17.76	18.14	51.38	3.80	28.17	10.600	0.0570	21.51	17.569

[a] CHNS analysis
[b] S_{BET}, BET surface area
[c] V_p, total pore volume
[d] D_p, average pore diameter

residues and heavy carbonaceous species, most probably by graphitic coke. The shell structure is composed of graphitic carbon with some defect sites, as confirmed by TEM analysis (Fig. 15). The weight loss between 80 and 120 °C is ascribed to the loss of surface hydroxyls and physically or chemically linked water from all samples, which was supported by their DTG endothermic peaks [82]. The first derivative of TGA curves (DTG) in Fig. 12 (c) presented the highest weight reduction rate for all catalysts with higher intensities for catalysts with metals occurred at below 100 °C, whereas it was significantly higher for TiCa at ~750 °C min and N/TiCa at ~450 °C. Primary pyrolysis processes occur on cellulose at low-temperature ranges. In this stage, monomeric phenols undergo side-chain reactions, ether bond cleavage, and evaporation. Methoxy group bonds are broken down, and aromatic rings are broken down and condensed during the secondary pyrolysis events, which take place above 400 °C [83,84]. However, DTG curves show that the peaks of TiCa and N/TiCa became more considerable than that of Pd and La, indicating that the introduction of Pd and La into the catalyst can considerably affect the reforming and pyrolysis reaction behavior of phenol and cellulose. The catalyst sintering and carbon deposition behaviors are low in NLP/TiCa and NL/TiCa, whereas the TiCa catalyst deactivation is caused by carbon deposition rather than the metal sintering, but N/TiCa displays severe sintering and carbon formation performances. Generally speaking, the total weight losses of TiCa, N/TiCa, NL/TiCa, and NLP/TiCa were 72.31%, 61.36%, 61.36%, and 51.38%, respectively; which are in line with the carbon content from CHNS analysis (13.8%, 9.6%, 4.1%, and 3.8%, respectively). Most of the carbon combustion happens at the WL_2 region, indicating an exothermic process consistent with oxidation. The breakdown of C═O groups on the surface of carbon-based catalysts may also be responsible for the weight loss over 700 °C [85]. The carbon deposition side reaction of the TiCa

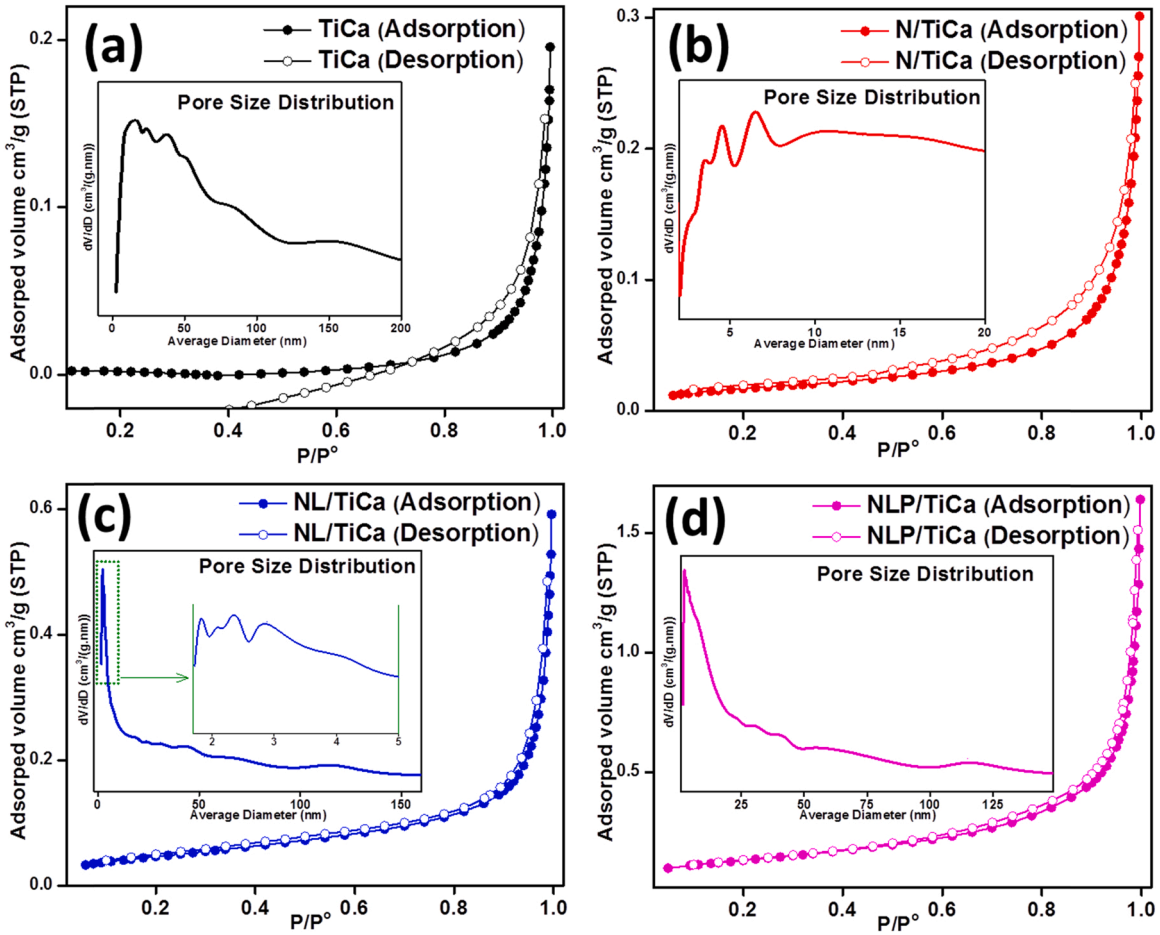

Fig. 13. Nitrogen adsorption isotherm and pore size distribution of the used (a) TiCa, (b) N/TiCa, (c) NL/TiCa, and (d) NLP/TiCa nano-catalysts.

and N/TiCa catalysts is also related to the higher acidity of those samples, as described in NH_3-TPD and Pyridine-FTIR spectra in Fig. 7.

The spent catalysts were also examined by BET surface area and N_2 adsorption-desorption isotherm, and the results are depicted in Table 3 and Fig. 13. As displayed in Table 3, the surface area of the spent catalysts employed in this work was considerably decreased compared to that of the fresh samples, most probably because of thermal sintering and carbon deposition. The S_{BET} of spent TiCa, N/TiCa, NL/TiCa, and NLP/TiCa nanocatalysts were 0.131, 1.39, 3.89, and 10.6 m^2/g, respectively. However, the highest surface area remains for the NLP/TiCa nanocatalyst with more porosity and active sites than those other samples. This sample with Pd NPs showed the most increased catalytic activity (Fig. 9) and lowest carbon deposition (). These results also indicate that the catalysts with Pd NPs are more competitive for recovering the textural characteristics of the spent samples. The results revealed that the H4 type isotherms loop remained unchanged for all catalysts with transition and noble metals NPs with pore size distribution in the range of 2–25 nm after the reaction, demonstrating the collapse of the mesoporous framework was not pronounced. These results indicated that adding Pd is beneficial to keeping the catalyst's activity and improving the catalyst's anti-coking performance.

Furthermore, a qualitative analysis of coke structures on the spent catalysts was conducted using FTIR spectroscopy. The two key bond vibration areas in the FTIR spectra of complete coke deposited on TiCa, N/TiCa, NL/TiCa, and NLP/TiCa nano-catalysts are shown in Fig. 14. While the vibrations in the area of 1650–1350 cm^{-1} belong to aromatics and specific bending modes of aliphatics, the vibrations in the 3200–2700 cm^{-1} essentially correspond to olefins (asymmetric and symmetric stretching) and monocyclic aromatics (olefins). Specifically, the IR bands at 586 cm^{-1}, 864 cm^{-1}, and 957 cm^{-1} are designated to functional groups of amide VI species, =CH bending out of the plane, and C–O symmetrical structure in aliphatic nature of coke, respectively. The single shoulder for the N/TiCa nanocatalyst at around 1265 cm^{-1} is ascribed to the −C–O single bond vibration of −C–OH group. The parent peaks at 1443 cm^{-1}, which can approve the presence of skeleton vibration of the pyrrole ring and C═C stretching [86] clearly indicating it is strengthened in this trend TiCa<Ni/TiCa<NL/TiCa<NLP/TiCA. Thus, pyrrole ring and C═C stretching are assigned to the catalyst with higher weight loss and lower catalytic performance. These peaks might also correspond to the asymmetric stretch vibration of CO_3^{2-} molecules [87]. The characteristic peaks at 1635 cm^{-1} correspond to the adsorbed H_2O molecules at the spent catalysts, whereas the 1805 cm^{-1} single bans for the NLP/TiCa sample are ascribed to the C= O stretching modes. The

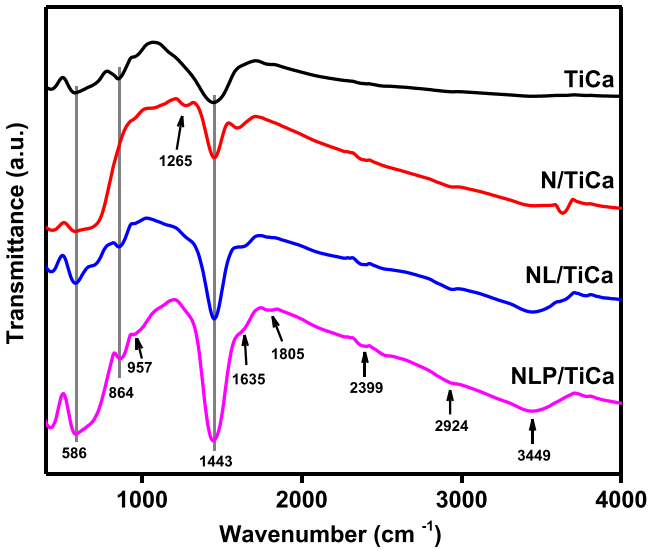

Fig. 14. Fourier transform infrared (FTIR-KBr) profiles of the used catalysts.

FTIR peaks at 2399 cm^{-1}, 2924 cm^{-1}, and 3449 cm^{-1} wavenumbers for the spent catalysts with transition and noble metals were equivalent to the linearly adsorbed O═C═O species [88], asymmetric stretching vibration of C−H [89], at ascribed to the O–H stretching vibration [90, 91], respectively. However, the intensities of those peaks were increased in the spent catalysts with transition and noble metals, which is evidence for decreasing monomeric phenols via successive C–O bond cleavage.

TEM images of the spent NLP/TiCa sample after 72 h time on stream are revealed in Fig. 15. After the in-situ pyrolysis-catalytic steam reforming reaction, the basic morphologies of the NLP/TiCa catalyst are retained, agreeing with the preferable performance and stability during the reaction; along with some smaller microparticles placed on the surface of the larger cuboid particles. The substances may identify Coke deposits with non-uniformly shaped particles shown in the photos. The coke deposits' disorganized structure matches that of amorphous coke exactly. The deposited carbon appears as the core-shell structure on the catalyst particles can be ascribed to the encapsulated graphitic carbon with a shell of 15 nm. The two factors responsible for this carbon production are carbon development on the surface of nickel and lanthanum catalysts and carbon diffusion via transition metal particle surfaces. This sort of carbon causes transition metal active sites to have weaker coke covering, which results in active metallic particles still being in contact with the gas flow and delaying the catalyst's deactivation [92].

4. Conclusion

This research revealed the synergistic influence of Pd, Ni, and TiCa support for hydrogen and valuable liquid generation from cellulose biopolymer wastes dissolved in phenol. To increase this study's feasibility and the cellulose ratio to solvent ratio, we modified the experimental setup and added a Parr Benchtop Reactor. This modification allows the quickly liquefying and rising of the amount of polymer and plastic waste in the reaction without causing line blockage. Four catalysts were prepared through hydrothermal and impregnation techniques: TiCa, N/TiCa, NL/TiCa, and NLP/TiCa nanocatalysts. The physicochemical characteristics of the fresh catalysts were examined by XRD, BET, N_2 adsorption-desorption isotherm, NH_3-TPD, IR-Pyridine, IR-Pyrrole, H_2-TPR, CO_2-TPD, FTIR-KBr, TEM, EDX, HRTEM, SAED, EDX, and ICP test and the used catalysts were characterized by TGA-DTG, BET, TEM, FTIR-KBr and CHNS. The best catalytic interaction between Pd, Ni, La, and TiCa was observed for the trimetallic NLP/TiCa nanocatalyst, which showed the highest catalytic activity at 600 °C compared to monometallic N/TiCa and bimetallic NL/TiCa catalysts, with high stability for 72 h of time on stream, almost complete phenol conversion (98.7%), and 99.6% of H_2 yield at 800 °C. The increased catalytic performance under the NLP/TiCa nanocatalyst can be ascribed to the increased surface area, metal support interaction, basicity, and active metal distribution of the synthesized catalyst as analyzed by BET surface area, H_2-TPR, CO_2-TPD, and EDX. The addition of Pd in the NL/TiCa increased the reducibility properties of the catalyst; therefore, a Ca*Ti, Pd*La, La*Ti, and La*Ni interaction exist as proven by XRD result for $LaPd_5$, $LaNi_5$, $La_{2.32}O_{12}Ti_4$, and $Ca(TiO_3)$ alloys. Carbon deposition was not considered the only reason for the low performance for TiCa and N/TiCa nanocatalysts. The catalyst sintering and carbon deposition behaviors are low in NLP/TiCa and NL/TiCa, whereas the TiCa catalyst deactivation is caused by carbon deposition rather than the metal sintering, but N/TiCa displays severe sintering and carbon formation performances. The carbon deposition side reaction of the TiCa and N/TiCa catalysts is also related to the higher acidity of those samples, as described in NH_3-TPD and Pyridine-FTIR spectra. The material balance also determined all the condensed hydrocarbons. The deposited coke appears as either large amorphous and graphitic with catalyst particles or as a rather uniform carbon coating that covers the catalyst particles. The liquid product compounds produced mainly from the thermal cracking of cellulose in almost all samples were ethanol, toluene, phenol, 2,4-dimethyl-benzo[*h*]quinoline, and hexadecane. The current study will

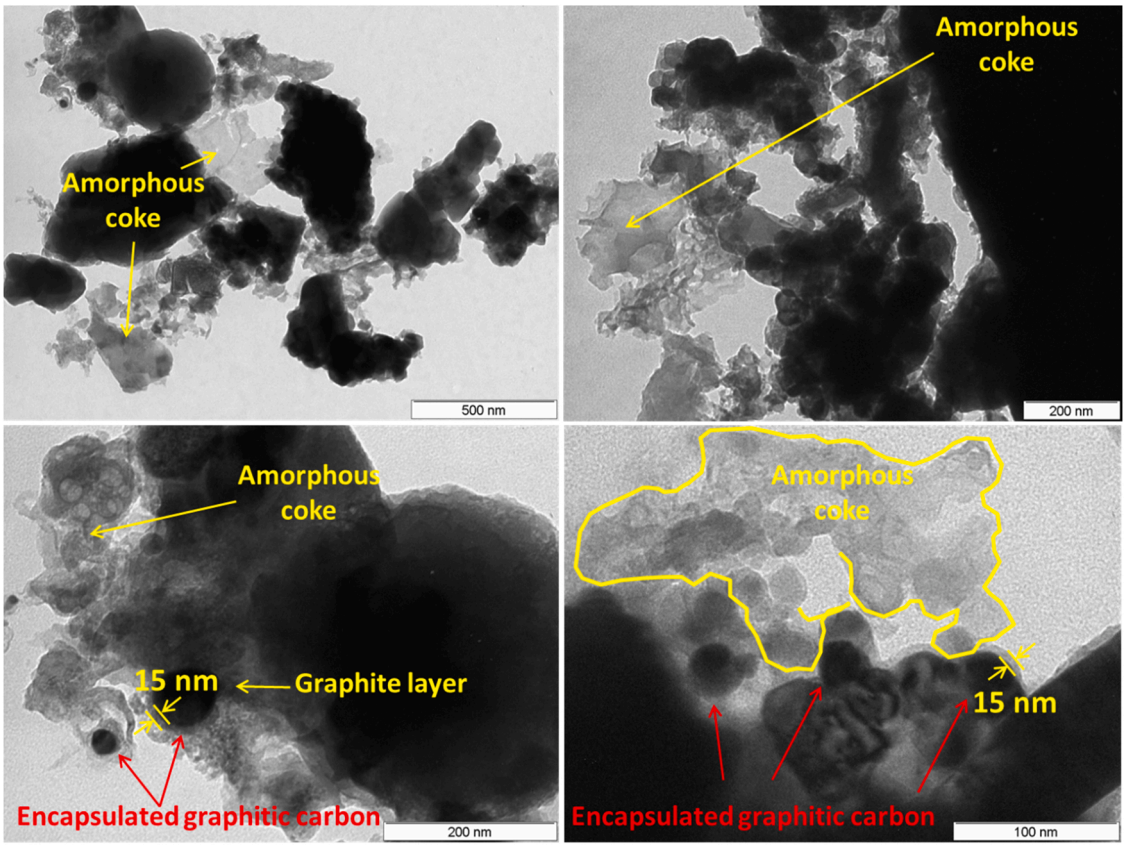

Fig. 15. TEM images of NLP/TiCa nanocatalysts.

offer an industrial basis for synthesizing effective trimetallic nanosized catalysts and help in the operative utilization of cellulose biopolymer waste and phenolic compounds for liquid fuel and hydrogen gas production.

CRediT authorship contribution statement

W. Nabgan: Writing, Experimental and characterization, T.A. Tuan Abdullah: Supervision and Methodology, M. Ikram: Writing and characterization, A.H.K. Owgi: Writing & English editing, A.H. Hatta: Writing tasks of the experimental part, M. Alhassan: Writing tasks of the reaction and stability parts, F.F.A. Aziz: Figures development and English editing, A.A. Jalil: English editing and characterization, T.V. Tran: Writing & English revision, R. Djellabi: Writing & English editing.

Declaration of Competing Interest

The authors declare that they have no known competing financial interests or personal relationships that could have appeared to influence the work reported in this paper.

Data Availability

No data was used for the research described in the article.

Acknowledgments

The primary author, Walid Nabgan, is grateful for the support from Universitat Rovira i Virgili under the Maria Zambrano Programme (Reference number: 2021URV-MZ-10). The authors are also grateful for the support given by Universiti Teknologi Malaysia (UTM) allocation budget in Pusat Pengurusan Makmal Universiti (PPMU) laboratory.

Appendix A. Supporting information

Supplementary data associated with this article can be found in the online version at doi:10.1016/j.jece.2023.109311.

References

[1] C. Maraveas, Environmental sustainability of greenhouse covering materials, Sustainability 11 (21) (2019).
[2] C. Maraveas, Production of sustainable and biodegradable polymers from agricultural waste, Polymers 12 (5) (2020).
[3] D. Chen, D. Lawton, M.R. Thompson, Q. Liu, Biocomposites reinforced with cellulose nanocrystals derived from potato peel waste, Carbohydr. Polym. 90 (1) (2012) 709–716.
[4] M.R. Kosseva, S. Zhong, M. Li, J. Zhang, N.A.S. Tjutju, Biopolymers produced from food wastes: a case study on biosynthesis of bacterial cellulose from fruit juices, in: M.R. Kosseva, C. Webb (Eds.), Food Industry Wastes, second ed., Academic Press, 2020, pp. 225–254.
[5] G. Vicente, J. Aguado, D.P. Serrano, N. Sánchez, HDPE chemical recycling promoted by phenol solvent, J. Anal. Appl. Pyrolysis 85 (1) (2009) 366–371.
[6] O. Primo, M.J. Rivero, I. Ortiz, A. Irabien, Mathematical modelling of phenol photooxidation: kinetics of the process toxicity, Chem. Eng. J. 134 (1) (2007) 23–28.
[7] Yang, J., and Li, Y.-P. Orthogonal Relief Algorithm for Feature Selection. *Proc., Intelligent Computing*, Springer Berlin Heidelberg, 227–234.
[8] W.W. Anku, M.A. Mamo, P.P. Govender, Phenolic compounds in water: sources, reactivity, toxicity and treatment methods, Phenolic Compd. -Nat. Sources, Import. Appl. (2017) 419–443.
[9] T. Abbas, M. Tahir, N.A. Saidina Amin, Enhanced metal–support interaction in Ni/Co3O4/TiO2 nanorods toward stable and dynamic hydrogen production from phenol steam reforming, Ind. Eng. Chem. Res. 58 (2) (2019) 517–530.
[10] W. Nabgan, T. Tuan Abdullah, R. Mat, B. Nabgan, Y. Gambo, A. Johari, Evaluation of reaction parameters of the phenol steam reforming over Ni/Co on ZrO2 using the full factorial experimental design, Appl. Sci. 6 (8) (2016) 223.
[11] D.S. Fardhyanti, N.A.C. Imani, A. Damayanti, S.N. Mardhotillah, M. Afifudin, A. Mulyaningtyas, A.E. Akhir, W. Nuramalia, P. Maulana, The separation of phenolic compounds from bio-oil produced from pyrolysis of corncobs, AIP Conf. Proc. 2243 (1) (2020), 020005.

[12] J.S. Moura, M.O.G. Souza, J.D.A. Bellido, E.M. Assaf, M. Opportus, P. Reyes, M. d C. Rangel, Ethanol steam reforming over rhodium and cobalt-based catalysts: effect of the support, Int. J. Hydrog. Energy 37 (4) (2012) 3213–3224.
[13] T. de Freitas Silva, J.A.C. Dias, C.G. Maciel, J.M. Assaf, Ni/Al2O3 catalysts: effects of the promoters Ce, La and Zr on the methane steam and oxidative reforming reactions, Catal. Sci. Technol. 3 (3) (2013) 635–643.
[14] K.S. Baamran, M. Tahir, M. Mohamed, A. Hussain Khoja, Effect of support size for stimulating hydrogen production in phenol steam reforming using Ni-embedded TiO2 nanocatalyst, J. Environ. Chem. Eng. 8 (1) (2020), 103604.
[15] K.S. Baamran, M. Tahir, Ni-embedded TiO2-ZnTiO3 reducible perovskite composite with synergistic effect of metal/support towards enhanced H2 production via phenol steam reforming, Energy Convers. Manag. 200 (2019), 112064.
[16] W. Nabgan, T.A. Tuan Abdullah, R. Mat, B. Nabgan, Y. Gambo, S. Triwahyono, Influence of Ni to Co ratio supported on ZrO2 catalysts in phenol steam reforming for hydrogen production, Int. J. Hydrog. Energy 41 (48) (2016) 22922–22931.
[17] J. Yan, R. Liu, Z. Li, P. Fu, P. Geng, W. Yi, Gas-phase catalytic hydrodeoxygenation of phenolic compounds derived from lignin pyrolysis for hydrocarbon production using Ni@HZSM-5-γ-Al2O3, J. Anal. Appl. Pyrolysis 166 (2022), 105626.
[18] M.C. Ramos, A.I. Navascués, L. García, R. Bilbao, Hydrogen production by catalytic steam reforming of acetol, a model compound of bio-oil, Ind. Eng. Chem. Res. 46 (8) (2007) 2399–2406.
[19] E. Akiki, D. Akiki, C. Italiano, A. Vita, R. Abbas-Ghaleb, D. Chlala, G. Drago Ferrante, M. Laganà, L. Pino, S. Specchia, Production of hydrogen by methane dry reforming: a study on the effect of cerium and lanthanum on Ni/MgAl2O4 catalyst performance, Int. J. Hydrog. Energy 45 (41) (2020) 21392–21408.
[20] M.A. Elharati, K.-M. Lee, S. Hwang, A. Mohammed Hussain, Y. Miura, S. Dong, Y. Fukuyama, N. Dale, S. Saunders, T. Kim, S. Ha, The effect of silica oxide support on the catalytic activity of nickel-molybdenum bimetallic catalyst toward ethanol steam reforming for hydrogen production, in: Chemical Engineering Journal, 441, 2022.
[21] J.L. Contreras, A. Figueroa, B. Zeifert, J. Salmones, G.A. Fuentes, T. Vázquez, D. Angeles, L. Nuño, Production of hydrogen by ethanol steam reforming using Ni–Co-ex-hydrotalcite catalysts stabilized with tungsten oxides, Int. J. Hydrog. Energy 46 (9) (2021) 6474–6493.
[22] M. Kushida, A. Yamaguchi, M. Miyauchi, Photocatalytic dry reforming of methane by rhodium supported monoclinic TiO2-B nanobelts, J. Energy Chem. 71 (2022) 562–571.
[23] G. Modragón-Galicia, M. Toledo Toledo, F. Morales-Anzures, P. Salinas-Hernández, A. Gutiérrez-Martínez, M.E.F. García, F. Tzompantzi, A. Barrera, J. Reyna-Alvarado, O.A. López-Galán, M. Ramos, R. Pérez-Hernández, Catalytic aspects of Pt/Pd supported on ZnO rods for hydrogen production in methanol steam reforming, Top. Catal. (2022).
[24] S. Aouad, C. Gennequin, M. Mrad, H.L. Tidahy, J. Estephane, A. Aboukaïs, E. Abi-Aad, Steam reforming of methanol over ruthenium impregnated ceria, alumina and ceria–alumina catalysts, Int. J. Energy Res. 40 (9) (2016) 1287–1292.
[25] W. Nabgan, B. Nabgan, T.A. Tuan Abdullah, M. Ikram, A.H. Jadhav, A.A. Jalil, M. W. Ali, Highly active biphasic anatase-rutile Ni-Pd/TNPs nanocatalyst for the reforming and cracking reactions of microplastic waste dissolved in phenol, ACS Omega 7 (4) (2022) 3324–3340.
[26] B. Nabgan, W. Nabgan, T.A. Tuan Abdullah, M. Tahir, Y. Gambo, M. Ibrahim, W. Syie Luing, Parametric study on the steam reforming of phenol-PET solution to hydrogen production over Ni promoted on Al2O3-La2O3 catalyst, Energy Convers. Manag. 142 (2017) 127–142.
[27] W. Nabgan, B. Nabgan, T.A. Tuan Abdullah, H. Alqaraghuli, N. Ngadi, A.A. Jalil, B. M. Othman, A.M. Ibrahim, T.J. Siang, Ni–Pt/Al nano-sized catalyst supported on TNPs for hydrogen and valuable fuel production from the steam reforming of plastic waste dissolved in phenol, Int. J. Hydrog. Energy 45 (43) (2020) 22817–22832.
[28] L. Han, Q. Liu, Y. Zhang, K. Lin, G. Xu, Q. Wang, N. Rong, X. Liang, Y. Feng, P. Wu, K. Ma, J. Xia, C. Zhang, Y. Zhong, A novel hybrid iron-calcium catalyst/absorbent for enhanced hydrogen production via catalytic tar reforming with in-situ CO_2 capture, Int. J. Hydrog. Energy 45 (18) (2020) 10709–10723.
[29] B. Tahir, M. Tahir, N.A.S. Amin, Tailoring performance of La-modified TiO2 nanocatalyst for continuous photocatalytic CO_2 reforming of CH4 to fuels in the presence of H2O, Energy Convers. Manag. 159 (2018) 284–298.
[30] M. Tahir, B. Tahir, Z.Y. Zakaria, A. Muhammad, Enhanced photocatalytic carbon dioxide reforming of methane to fuels over nickel and montmorillonite supported TiO2 nanocomposite under UV-light using monolith photoreactor, J. Clean. Prod. 213 (2019) 451–461.
[31] W. Nabgan, B. Nabgan, M. Ikram, A.H. Jadhav, M.W. Ali, A. Ul-Hamid, H. Nam, P. Lakshminarayana, k Ankit, M.B. Bahari, N.F. Khusnun, Synthesis and catalytic properties of calcium oxide obtained from organic ash over a titanium nanocatalyst for biodiesel production from dairy scum, Chemosphere 290 (2022), 133296.
[32] F.M. Alptekin, M.S. Celiktas, Review on catalytic biomass gasification for hydrogen production as a sustainable energy form and social, technological, economic, environmental, and political analysis of catalysts, ACS Omega 7 (29) (2022) 24918–24941.
[33] G. Wu, C. Zhang, S. Li, Z. Han, T. Wang, X. Ma, J. Gong, Hydrogen production via glycerol steam reforming over Ni/Al2O3: influence of nickel precursors, ACS Sustain. Chem. Eng. 1 (8) (2013) 1052–1062.
[34] H. Yu, T. Ma, Y. Shen, D. Chen, Experimental study on catalytic effect of biomass pyrolysis volatile over nickel catalyst supported by waste iron slag. Int. J. Energy Res. 41 (14) (2017) 2063–2073.
[35] W. Nabgan, T.A. Tuan Abdullah, R. Mat, B. Nabgan, S. Triwahyono, A. Ripin, Hydrogen production from catalytic steam reforming of phenol with bimetallic nickel-cobalt catalyst on various supports, Appl. Catal. A Gen. 527 (2016) 161–170.
[36] W. Nabgan, T.A.T. Abdullah, R. Mat, B. Nabgan, A.A. Jalil, L. Firmansyah, S. Triwahyono, Production of hydrogen via steam reforming of acetic acid over Ni and Co supported on La2O3 catalyst, Int. J. Hydrog. Energy 42 (14) (2017) 8975–8985.
[37] G. Del Angel, A. Bonilla, Y. Peña, J. Navarrete, J.L.G. Fierro, D.R. Acosta, Effect of lanthanum on the catalytic properties of PtSn/γ-Al2O3 bimetallic catalysts prepared by successive impregnation and controlled surface reaction, J. Catal. 219 (1) (2003) 63–73.
[38] M. Sait Izgi, M.Ş. Ece, H.Ç. k Kazici, Ö. Şahïn, E. Onat, Hydrogen production by using Ru nanoparticle decorated with Fe3O4@SiO2–NH2 core-shell microspheres, Int. J. Hydrog. Energy 45 (55) (2020) 30415–30430.
[39] L. Li, L. Zhou, S. Ould-Chikh, D.H. Anjum, M.B. Kanoun, J. Scaranto, M.N. Hedhili, S. Khalid, P.V. Laveille, L. D'Souza, A. Clo, J.-M. Basset, Controlled surface segregation leads to efficient coke-resistant nickel/platinum bimetallic catalysts for the dry reforming of methane, ChemCatChem 7 (5) (2015) 819–829.
[40] S.A. Theofanidis, V.V. Galvita, M. Sabbe, H. Poelman, C. Detavernier, G.B. Marin, Controlling the stability of a Fe–Ni reforming catalyst: structural organization of the active components, Appl. Catal. B Environ. 209 (2017) 405–416.
[41] A.-J. Wang, F.-F. Li, J.-N. Zheng, H.-X. Xi, Z.-Y. Meng, J.-J. Feng, Green synthesis of porous flower-like palladium with high electrocatalytic activity towards methanol oxidation, RSC Adv. 3 (26) (2013) 10355–10362.
[42] B. Nabgan, M. Tahir, T.A.T. Abdullah, W. Nabgan, Y. Gambo, R. Mat, I. Saeh, Ni/Pd-promoted Al2O3–La2O3 catalyst for hydrogen production from polyethylene terephthalate waste via steam reforming, Int. J. Hydrog. Energy 42 (16) (2017) 10708–10721.
[43] W. Nabgan, B. Nabgan, T.A. Tuan Abdullah, N. Ngadi, A.A. Jalil, N.S. Hassan, S. M. Izan, W.S. Luing, S.N. Abdullah, F.S.A. Majeed, Conversion of polyethylene terephthalate plastic waste and phenol steam reforming to hydrogen and valuable liquid fuel: Synthesis effect of Ni–Co/ZrO2 nanostructured catalysts, Int. J. Hydrog. Energy 45 (11) (2020) 6302–6317.
[44] W. Nabgan, B. Nabgan, T.A. Tuan Abdullah, A.A. Jalil, A. Ul-Hamid, M. Ikram, A. H. Nordin, A. Coelho, Production of hydrogen and valuable fuels from polyethylene terephthalate waste dissolved in phenol reforming and cracking reactions via Ni-Co/CeO2 nano-catalyst, J. Anal. Appl. Pyrolysis 154 (2021), 105018.
[45] W. Nabgan, B. Nabgan, T.A.T. Abdullah, M. Ikram, A.H. Jadhav, M.W. Ali, A. A. Jalil, Hydrogen and value-added liquid fuel generation from pyrolysis-catalytic steam reforming conditions of microplastics waste dissolved in phenol over bifunctional Ni-Pt supported on Ti-Al nanocatalysts, Catal. Today 400–401 (1) (2022) 35–48.
[46] J.H. Park, C. Park, K.S. Lee, S.J. Suh, Effect of NaOH and precursor concentration on size and magnetic properties of FeCo nanoparticles synthesized using the polyol method, AIP Adv. 10 (11) (2020), 115220.
[47] Z.A. Alothman, A review: fundamental aspects of silicate mesoporous materials, Materials 5 (12) (2012) 2874–2902.
[48] S. Yurdakal, C. Garlisi, L. Özcan, M. Bellardita, G. Palmisano, (Photo)catalyst characterization techniques: adsorption isotherms and BET, SEM, FTIR, UV–Vis, photoluminescence, and electrochemical characterizations, in: G. Marcì, L. Palmisano (Eds.), Heterogeneous Photocatalysis, Elsevier, 2019, pp. 87–152.
[49] P.I. Ravikovitch, A.V. Neimark, Characterization of nanoporous materials from adsorption and desorption isotherms. Colloids Surf. A: Physicochem. Eng. Asp. 187–188 (2001) 11–21.
[50] A. Sayari, H.T. Wang, J.G. Goodwin, Surface structure dependence of reversible/weak H2 chemisorption on supported Ru, J. Catal. 93 (2) (1985) 368–374.
[51] I. Prymak, V.N. Kalevaru, S. Wohlrab, A. Martin, Continuous synthesis of diethyl carbonate from ethanol and CO_2 over Ce–Zr–O catalysts. Catal. Sci. Technol. 5 (4) (2015) 2322–2331.
[52] H. Liu, S. Xu, G. Zhou, K. Xiong, Z. Jiao, S. Wang, CO_2 hydrogenation to methane over Co/KIT-6 catalysts: effect of Co content, Fuel 217 (2018) 570–576.
[53] M. Zhang, J. Zhang, Y. Wu, J. Pan, Q. Zhang, Y. Tan, Y. Han, Insight into the effects of the oxygen species over Ni/ZrO2 catalyst surface on methane reforming with carbon dioxide, Appl. Catal. B: Environ. 244 (2019) 427–437.
[54] J. Saupsor, C. Pei, H. Li, S. Wongsakulphasatch, P. Kim-Lohsoontorn, S. Ratchahat, W. Kiatkittipong, S. Assabumrungrat, J. Gong, Bifunctional catalyst NiFe–MgAl for hydrogen production from chemical looping ethanol reforming, Energy Fuels 35 (14) (2021) 11580–11592.
[55] O. Cairon, E. Dumitriu, C. Guimon, Acido-basicity of Mg−Ni−Al mixed oxides from LDH precursors: a FTIR and XPS study, J. Phys. Chem. C. 111 (22) (2007) 8015–8023.
[56] M.A.A. Aziz, A.A. Jalil, S. Triwahyono, R.R. Mukti, Y.H. Taufiq-Yap, M.R. Sazegar, Highly active Ni-promoted mesostructured silica nanoparticles for CO_2 methanation, Appl. Catal. B Environ. 147 (2014) 359–368.
[57] S. Echeandia, B. Pawelec, V.L. Barrio, P.L. Arias, J.F. Cambra, C.V. Loricera, J.L. G. Fierro, Enhancement of phenol hydrodeoxygenation over Pd catalysts supported on mixed HY zeolite and Al2O3. An approach to O-removal from bio-oils. Fuel 117 (2014) 1061–1073.
[58] H. Li, Y. Wang, F. Meng, H. Chen, C. Sun, S. Wang, Direct synthesis of high-silica nano ZSM-5 aggregates with controllable mesoporosity and enhanced catalytic properties. RSC Adv. 6 (101) (2016) 99129–99138.
[59] S. Yue, B. Wu, Z. Cao, L. Zhou, Z. Yin, X. Zou, X. Wang, X. Zou, X. Lu, Cobalt promoted molybdenum carbide supported on γ-alumina as an efficient catalyst for hydrodesulfurization of dibenzothiophene, J. Clean. Prod. (2022), 133642.
[60] R.M. Gendreau, R. Burton, The KBr pellet: a useful technique for obtaining infrared spectra of inorganic species, Appl. Spectrosc. 33 (6) (1979) 581–584.

[61] S.J. Han, Y. Bang, J. Yoo, J.G. Seo, I.K. Song, Hydrogen production by steam reforming of ethanol over mesoporous Ni–Al2O3–ZrO2 xerogel catalysts: effect of nickel content, Int. J. Hydrog. Energy 38 (20) (2013) 8285–8292.
[62] C. Pizzolitto, F. Menegazzo, E. Ghedini, G. Innocenti, A. Di Michele, M. Mattarelli, G. Cruciani, F. Cavani, M. Signoretto, Ethanol steam reforming on lanthanum Ni-ZrO2 catalysts, ACS Sustain. Chem. Eng. 8 (29) (2020) 10756–10766.
[63] G. Bekiaris, C. Peltre, L.S. Jensen, S. Bruun, Using FTIR-photoacoustic spectroscopy for phosphorus speciation analysis of biochars, Spectrochim. Acta Part A Mol. Biomol. Spectrosc. 168 (2016) 29–36.
[64] D.J. Ahn, A. Berman, D. Charych, Probing the dynamics of template-directed calcite crystallization with in Situ FTIR, J. Phys. Chem. 100 (30) (1996) 12455–12461.
[65] A.Y. Waziri, A.A. Osigbesan, F.N. Dabai, S.M. Shuwa, A.Y. Atta, B.Y. Jibril, Catalytic reforming of gaseous products from pyrolysis of low-density polyethylene over iron-modified ZSM-5 catalysts, Appl. Petrochem. Res. 9 (2) (2019) 101–112.
[66] A. Kellenberger, E. Dmitrieva, L. Dunsch, Structure dependence of charged states in "linear" polyaniline as studied by In Situ ATR-FTIR spectroelectrochemistry, J. Phys. Chem. B 116 (14) (2012) 4377–4385.
[67] S. Suresh, S. Karthikeyan, K. Jayamoorthy, FTIR and multivariate analysis to study the effect of bulk and nano copper oxide on peanut plant leaves. J. Sci.: Adv. Mater. Devices 1 (3) (2016) 343–350.
[68] Zhang, Y., Zhang, L., Han, C., Ren, Y., Ji, Y., Ge, Y., Li, Z., and He, J. (2022). "Preparation, characteristics and mechanisms of Cd(II) adsorption from aqueous solution by mango kernel-derived biochar." *Biomass Conversion and Biorefinery*.
[69] F.J. Stevenson, Humus chemistry: genesis, composition, reactions, John Wiley & Sons, 1994.
[70] E.A. Glascoe, J.M. Zaug, M.R. Armstrong, J.C. Crowhurst, C.D. Grant, L.E. Fried, Nanosecond time-resolved and steady-state infrared studies of photoinduced decomposition of TATB at ambient and elevated pressure, J. Phys. Chem. A 113 (20) (2009) 5881–5887.
[71] L.-X. You, Y.-M. Fang, J.-W. Guo, L. Zhang, J.-S. Chen, J.-J. Sun, Mechanism of electro-catalytic oxidation of shikimic acid on Cu electrode based on in situ FTIRS and theoretical calculations, Electrochim. Acta 58 (2011) 165–171.
[72] C. Khoury, S. Holton, D. Shpasser, E. Hallo, A. Kulkarni, F.C. Jentoft, O.M. Gazit, Elucidating cooperative interactions between grafted amines and tin or titanium sites on silica, ACS Catal. 12 (16) (2022) 9846–9856.
[73] K. Zhang, Q. Meng, H. Wu, M. He, B. Han, Selective hydrogenolysis of 5-hydroxymethylfurfural into 2,5-dimethylfuran under mild conditions using Pd/MOF-808, ACS Sustain. Chem. Eng. 10 (31) (2022) 10286–10293.
[74] T. Muhizi, S. Grelier, V. Coma, Synthesis and antibacterial activity of aminodeoxyglucose derivatives against listeria innocua and Salmonella typhimurium, J. Agric. Food Chem. 57 (19) (2009) 8770–8775.
[75] D.A. Boyne, M.J. Varady, R.H. Lambeth, J.H. Eikenberg, S.A. Bringuier, T.P. Pearl, B.A. Mantooth, Solvent-assisted desorption of 2,5-lutidine from polyurethane films, J. Phys. Chem. B 122 (7) (2018) 2155–2164.
[76] S.E. Fenni, F. Bertella, O. Monticelli, A.J. Müller, N. Hadadoui, D. Cavallo, Renewable and tough poly(l-lactic acid)/polyurethane blends prepared by dynamic vulcanization, ACS Omega 5 (41) (2020) 26421–26430.
[77] J. Gandara-Loe, B.E. Souza, A. Missyul, G. Giraldo, J.C. Tan, J. Silvestre-Albero, MOF-based polymeric nanocomposite films as potential materials for drug delivery devices in ocular therapeutics, ACS Appl. Mater. Interfaces 12 (27) (2020) 30189–30197.
[78] S.A. Al-Hammadi, A.M. Al-Amer, T.A. Saleh, Alumina-carbon nanofiber composite as a support for MoCo catalysts in hydrodesulfurization reactions, Chem. Eng. J. 345 (2018) 242–251.
[79] Z. Zhang, Y. Wang, K. Sun, Y. Shao, L. Zhang, S. Zhang, X. Zhang, Q. Liu, Z. Chen, X. Hu, Steam reforming of acetic acid over Ni–Ba/Al2O3 catalysts: impacts of barium addition on coking behaviors and formation of reaction intermediates, J. Energy Chem. 43 (2020) 208–219.
[80] J. Pu, F. Ikegami, K. Nishikado, E.W. Qian, Effect of ceria addition on NiRu/CeO2Al2O3 catalysts in steam reforming of acetic acid, Int. J. Hydrog. Energy 42 (31) (2017) 19733–19743.
[81] Q. Xue, Z. Li, H. Yi, Z. Jiang, B. Yan, Y. Wang, G. Luo, Controlling sintering and carbon deposition with post-coated MgO confined group VIII metal-based catalysts towards durable high-temperature steam reforming, Appl. Catal. B Environ. (2022), 121874.
[82] S. Moloi, M.D. Farahani, A.S. Mahomed, S. Singh, H.B. Friedrich, The role of monomeric VOx supported on anatase in catalytic dehydrogenation of n-octane assisted by CO_2 addition, Mol. Catal. 530 (2022), 112578.
[83] H. Kawamoto, Lignin pyrolysis reactions, J. Wood Sci. 63 (2) (2017) 117–132.
[84] M. Parchami, S. Agnihotri, M.J. Taherzadeh, Aqueous ethanol organosolv process for the valorization of Brewer's spent grain (BSG), Bioresour. Technol. 362 (2022), 127764.
[85] Cheng, Z., Wang, Y., Jin, D., Liu, J., Wang, W., Gu, Y., Ni, W., Feng, Z., and Wu, M. (2022). "Petroleum pitch-derived porous carbon as a metal-free catalyst for direct propane dehydrogenation to propylene." *Catalysis Today*.
[86] H. Zheng, M. Chen, Y. Sun, B. Zuo, Self-Healing, Wet-Adhesion silk fibroin conductive hydrogel as a wearable strain sensor for underwater applications, Chem. Eng. J. 446 (2022), 136931.
[87] R. Madhuvilakku, R. Mariappan, S. Jeyapal, S. Sundar, S. Piraman, Transesterification of palm oil catalyzed by fresh water bivalve mollusk (margaritifera falcata) shell as heterogeneous catalyst, Ind. Eng. Chem. Res. 52 (49) (2013) 17407–17413.
[88] C.C. Chong, Y.W. Cheng, H.D. Setiabudi, N. Ainirazali, D.-V.N. Vo, B. Abdullah, Dry reforming of methane over Ni/dendritic fibrous SBA-15 (Ni/DFSBA-15): Optimization, mechanism, and regeneration studies, Int. J. Hydrog. Energy 45 (15) (2020) 8507–8525.
[89] D. Choi, S. Jung, Y.F. Tsang, H. Song, D.H. Moon, E.E. Kwon, Sustainable valorization of styrofoam and CO_2 into syngas. Sci. Total Environ. 834 (2022), 155384.
[90] M. Mokhatr Mohamed, H. El-Faramawy, An innovative nanocatalyst α-Fe2O3/AlOOH processed from gibbsite rubbish ore for efficient biodiesel production via utilizing cottonseed waste oil, Fuel 297 (2021), 120741.
[91] C.V. Rode, V.S. Kshirsagar, J.M. Nadgeri, K.R. Patil, Cobalt–salen intercalated montmorillonite catalyst for air oxidation of p-cresol under mild conditions, Ind. Eng. Chem. Res. 46 (25) (2007) 8413–8419.
[92] Z. Taherian, M. Yousefpour, M. Tajally, B. Khoshandam, Promotional effect of samarium on the activity and stability of Ni-SBA-15 catalysts in dry reforming of methane, Microporous Mesoporous Mater. 251 (2017) 9–18.